

THESIS

PATTERNS OF DUST-ENHANCED ABSORBED ENERGY AND SHIFTS IN MELT  
TIMING FOR SNOW OF SOUTHWESTERN COLORADO

Submitted by

Caroline R. Duncan

Department of Ecosystem Science and Sustainability

In partial fulfillment of the requirements

For the Degree of Master of Science

Colorado State University

Fort Collins, Colorado

Summer 2020

Master's Committee:

Advisor: Steven Fassnacht

Stephanie Kampf

Jay Ham

Copyright by Caroline Rosalie Duncan 2020

All Rights Reserved

## ABSTRACT

### PATTERNS OF DUST-ENHANCED ABSORBED ENERGY AND SHIFTS IN MELT TIMING FOR SNOW OF SOUTHWESTERN COLORADO

Deposited dust layers reduce the surface albedo of snow and accelerate melt by this change to the snowpack energy balance. Senator Beck Study Basin in the San Juan Mountains of southwestern Colorado monitors the effects of dust on midlatitude continental snowpack. Continuous automated measurements include shortwave and longwave radiation in addition to conventional micrometeorological variables. Dust layer characteristics and snow properties are collected during snow pit excavation throughout each ablation period. Both sets of data were used to simulate snowpack under observed and dust-free conditions with the snow energy balance model SNOBAL for WY2007 to WY2019. Across the 13 years, dust concentrations ranged from 0.16 to 4.80 mg g<sup>-1</sup> resulting in a range of daily mean dust-enhanced absorbed visible energy from 31 to 50 W m<sup>-2</sup> during ablation, with hourly peaks up to 347 W m<sup>-2</sup>. We found snow melt accelerated by 11 to 31 days in a logarithmic response to end-of-year dust concentration modified by seasonal variations in snow amount and cloud cover.

## ACKNOWLEDGEMENTS

This work would not have been possible without the expertise and stewardship of Jeff Derry, who serves as the current Director of the Center for Snow and Avalanche Studies. In this role, Jeff maintains the Senator Beck Study Basin and freely provides collected data to mountain snow hydrologists across the country. Over the course of my research, Jeff and his wife Kim have made me feel welcome in their home and shared much life wisdom over a succession of beverages.

I am also grateful to Micah Johnson and the team at the Northwest Watershed Research Center (USDA-ARS) in Boise, Idaho for their enthusiastic technical support. Micah devoted hours to teaching me how to run the snowpack energy balance model SNOBAL and was incredibly helpful over the month-long troubleshooting process. The rest of the office was frequently involved in answering questions and were unfailingly supportive throughout.

And to all the family, friends, colleagues, and mentors who gave me love, time, and guidance over the course of this research—thank you.

## TABLE OF CONTENTS

ABSTRACT .....	ii
ACKNOWLEDGEMENTS .....	iii
Chapter 1. Introduction .....	1
1.1 Background .....	1
1.2 Previous Work .....	3
1.3 Research Motivation .....	6
Chapter 2. Research Investigation .....	8
2.1. Introduction .....	8
2.1.1. Background .....	8
2.1.2. Research Objectives .....	8
2.2. Study Site and Datasets .....	9
2.2.1. Study Basin and Automated Data .....	9
2.2.2. Snowpack Development and Dust Timing .....	10
2.2.3. CSAS Snow Stake Data .....	10
2.2.4. CSAS Snow Pit Data .....	11
2.2.5. SNOTEL Site and Data .....	11
2.3. Methods .....	14
2.3.1. Albedo Corrections .....	14
2.3.2. Dust Concentrations .....	16
2.3.3. Absorbed Energy Calculations .....	16
2.3.4. Snow Energy Balance Model .....	17
2.4. Results .....	23
2.4.1. Daily Mean Visible DEAE .....	23
2.4.2. DEAE and Potential Drivers .....	24
2.4.3. Modeled SWE and Snow Cover Duration .....	26
2.4.4. Snow Cover Duration and Potential Drivers .....	27
2.5. Discussion .....	34
2.5.1. DEAE Calculations .....	34
2.5.2. Potential Drivers of DEAE .....	36
2.5.3. Modeling of Snow Cover .....	39
2.5.4. Potential Drivers of Snow Cover Duration .....	41
2.6. Conclusion .....	45
Chapter 3. Implications and Future Work .....	46
References .....	49
Appendix A. Datasets .....	54
Appendix B. Individual Model Results .....	55
Appendix C. Multiple Regression Analysis .....	57

## CHAPTER 1. INTRODUCTION

### 1.1. Background

More than 1/6 of the world's population depends on snowmelt-derived water resources (Barnett et al., 2005) and snow has significant effects on the energy balance of the planet (Domine et al., 2007). It is critical to better understand seasonal snow behavior and determine quantitative energy balance connections. The spatial distributions of snow albedo and snow water equivalent (SWE) are fundamental properties of mountain snowpack for understanding timing and magnitude of runoff (Painter et al., 2016). Snow albedo is a measure of snow surface reflectivity indicating how much solar radiation is reflected versus absorbed by the snowpack. The degree of scattering and the amount of absorption differ based on general wavelength (Marks and Dozier, 1992). Metamorphism of snow grains due to aging of the snowpack or stage of melt decreases snow albedo in the near-infrared (NIR, 0.7 to 1.5  $\mu\text{m}$ ) and shortwave-infrared wavelengths (SWIR, 1.5 to 3.0  $\mu\text{m}$ ) (Colbeck, 1982). Wiscombe and Warren (1980) developed an albedo decay model for pure snow which behaved similarly to observations in NIR wavelengths but in the visible spectrum modeled albedos that were consistently higher than observed which they attributed to deposition of atmospheric particulates within the snowpack. When at or near the snow surface, light-absorbing particulates (LAPs) such as mineral dust, black carbon, ash, or tree litter generally decrease snow albedo in the visible wavelengths (VIS, 0.4 to 0.7  $\mu\text{m}$ ) (Painter et al., 2012; Skiles et al., 2018). During melt in midlatitude continental mountain environments, the snow surface energy balance is dominated by solar radiation (Marks and Dozier,

1992; Oerlemans, 2000). The additional modification of LAPs to snow surface albedo could therefore be a significant driver of changes in snowpack energy balance and resulting melt.

The components of snow energy balance have been incorporated into snowpack models, yielding a better representation of snowpack processes and greater accuracy in simulating actual snow characteristics with more precise energy balance accounting. However, temperature-index models (e.g., SNOW17; Anderson, 1976) are commonly used in streamflow forecasting in snowmelt-dominated basins (Franz et al., 2008). These models use an empirical correlation between air temperature and snowmelt calibrated to the historical period of record (Hock, 2003) and are thus at risk of increasing uncertainty in an increasingly variable climate (Bryant et al., 2013; Painter et al., 2016). Follum et al. (2019) found that a modified temperature-index model produced more accurate estimates of snowmelt-derived streamflow than a temperature-index model. This modified temperature-index model replaced air temperature with a radiation-derived proxy temperature based on elevation, land cover, temperature, and cloud cover data and thus indirectly included both longwave and shortwave radiation components. However, the shortwave radiation component relied on a snow albedo term that only simulated changes from grain metamorphism and did not account for the effect of LAPs (Follum et al., 2015).

Variations in amount and timing of snow accumulation and ablation result in variations of both timing and amount of snow-derived water resources (e.g., Stewart et al., 2005; Barnhart et al., 2016; Harpold and Brooks, 2018). Worldwide, climate warming is expected to decrease high elevation snowpack more than potential winter

precipitation increases can offset (Stewart, 2009). A better understanding of the physical drivers of changes in snowmelt timing is necessary to adapt water resource management facing these projected decreases in total runoff amount. One physical driver of variations in snowmelt timing is the increased springtime energy forcing exerted by black carbon and mineral dust deposits on snowpack (e.g., Bales et al., 2006; Flanner et al., 2009). LAP emissions worldwide are projected to increase in frequency and magnitude and intensify effects on mountain snow systems already perturbed by climate warming (Painter et al., 2007). Since solar radiation is the largest energy input to seasonal snowcover at midlatitudes (Painter et al., 2016; Harpold and Brooks, 2018) and determines seasonal snow presence and persistence, it is critical to better understand LAP-induced changes in albedo and the implications for changes in snowmelt timing.

## **1.2. Previous Work**

The Southern Rocky Mountains of the western United States have a seasonal snowpack particularly sensitive to solar radiation inputs and climate challenges to regional water security have made the area a leading research location for understanding LAP impacts to seasonal snowcover (Painter et al., 2007; Skiles et al., 2018). Currently, the Southern Rocky Mountains have a continental snowpack regime characterized by a relatively lower peak SWE amount, longer accumulation periods, later onset of snowmelt, and lower rates of snowmelt than other North American snow regimes (Trujillo et al., 2014). The average date of peak SWE for Colorado occurs in mid-April (Serreze et al., 2001). Peak SWE amount sets a threshold for potential runoff magnitude but melt rate determines how much snowpack becomes streamflow,

indicating that melt magnitude estimates can be refined with a better understanding of melt timing (Fassnacht et al., 2017). Under a projected warming climate regime, decreases in SWE do not necessarily imply changes in snowmelt timing because of the significant relative contribution of latent and radiant energy fluxes to snowmelt (Harpold and Brooks, 2018). For the western US in general, timing and rate of snowmelt may control the partitioning between evapotranspiration (ET) and streamflow generation, with faster snowmelt corresponding to higher streamflow (Painter et al., 2010). Earlier melt initiation is connected to overall slower melt rates (Musselman et al., 2017) and lower streamflow volume (Barnhart et al., 2016).

Long-term net radiation data are necessary to determine physical drivers of changes in snowmelt rates. After the recommendation of Bales et al. (2006), a study basin was selected and instrumented in southwestern Colorado to capture a full suite of micrometeorological variables including longwave and shortwave radiation fluxes. Senator Beck Study Basin (SBB) has been maintained by Center for Snow and Avalanche Studies (CSAS) from 2005 to present and has generated a point-based record of hourly net radiation data in parallel with sub-monthly manual snow observations (Landry et al., 2014). SBB is located within the San Juan Mountains, which rise to the east of the Colorado Plateau and create an orographic barrier which captures storms blowing across this arid region (Lawrence et al., 2010). The region is considered to be in a mega-drought that is projected to continue (Williams et al., 2020). Increased wind erosion of the Colorado Plateau can cause elevated aeolian sediment transport (Nauman et al., 2018). Arid regions in Asia could supply some of the aeolian dust found in the San Juan snowpack, but there is strong evidence to support regional sources as

the source of most spring dust inputs (Lawrence et al., 2010; Reynolds et al., 2020). Variations in spatial dust deposition, concentration, and exposure timing yield large variation in snow albedo, which drives large variation in net radiation and resulting snowmelt rates for the Southern Rocky Mountains (Painter et al., 2017).

Skiles et al. (2012) compared different degree warming scenarios under climate change and found that air temperature increases could increase daily mean longwave irradiance and daily mean sensible heating, but these increases are smaller than dust-enhanced surface shortwave absorption for even seasons with low dust concentrations. The snow surface energy flux is dominated by dust radiative forcing to the extent that snowmelt rates during the rising limb of the Colorado River hydrograph are insensitive to changes in air temperature (Painter et al., 2017). Deems et al. (2013) found that variations in dust concentration can alter runoff volume, with “extreme” dust events capable of shifting peak snowmelt 3 weeks earlier for the Colorado River and directly reducing runoff by 1% with additional potential indirect losses from lengthened periods of ET and soil infiltration. Previous studies of SBB snowpack from 2005 through 2012 have found that deposited desert dust has shortened snow cover duration by 18 to 51 days (Painter et al., 2007; Skiles et al., 2012). Comparison of two sites within the Colorado River Basin show a spatial variability in dust loading and corresponding range of melt advancement which implies that SBB may be more heavily influenced by dust than the remainder of the basin (Skiles et al., 2015). SBB also has a clear dust signal compared to other potential LAPs: previous studies measured black carbon concentrations 4-6 orders of magnitude lower than dust concentrations, making it relatively negligible in LAP radiative forcing compared to such heavy dust loading

(Skiles and Painter, 2017; Skiles et al., 2018). Given the significant observed relation between dust loading and melt advancement at SBB for WY2005-2010 (Skiles et al., 2012) and for WY2005-2013 (Skiles et al., 2015), this project examines a longer period of record to characterize the range of radiative forcing from dust and identify interannual patterns.

### **1.3. Research Motivation**

Dust-on-snow modifications to the amount and timing of snowmelt for the Colorado River Basin need to be better characterized to understand broader operational consequences, especially for water resources management. Previous examinations of the potential uncertainty in streamflow forecasting when dust radiative forcing was not accounted for found a shift in runoff prediction bias of  $10.0\% \pm 1.5\%$  and a  $1.5 \pm 0.6$  day shift in runoff center of mass for every  $10 \text{ Wm}^{-2}$  change in dust forcing (Bryant et al., 2013). This is an additional refinement of the general trend across western North America for the latter half of the 20<sup>th</sup> century of increasing amounts of streamflow occurring 1-4 weeks earlier (Stewart et al., 2004; Clow, 2010; Harpold et al., 2012). Using just six years of data for SBB, the change in date of runoff center of mass at the Uncompahgre USGS gage was found to have a significant relation with dust-modified change in date of seasonal snow melt-out ( $R^2 = 0.75$ ) (Bryant et al., 2013). Variability in the date of maximum SWE is projected to increase (Marshall et al., 2019) which suggests that timing of runoff will become increasingly variable, although still dependent on melt rates and flow path processes such as ET. In general, snowmelt rates across the western US are projected to be slower and with an earlier onset (Musselman et al., 2017). Understanding the physical processes which control the timing and magnitude of

melt rates will improve streamflow simulation and forecasting (e.g. Bryant et al., 2013; Painter et al., 2017). It will be necessary to combine physical and operational models to more accurately represent energy fluxes to the snowpack (e.g., Harpold and Brooks, 2018; Follum et al., 2019). Latent heat and longwave radiation energy fluxes have a larger relative contribution to snowpack loading at humid sites such as the Pacific Northwest than at arid or semi-arid sites such as the Intermountain West (Harpold and Brooks, 2018). These drier sites are thus more sensitive to solar radiation energy inputs and are also more likely to experience higher winter sublimation losses (Sexstone et al., 2016), earlier melt initiation (Trujillo and Molotch, 2014), slower melt rates (Fassnacht et al., 2017), and lower streamflow (Barnhart et al., 2016) under projected climate changes. Better understanding of these factors in combination with snowmelt timing changes due to dust would improve operational streamflow forecast ability.

This research seeks to characterize how much additional energy is absorbed by the snowpack due to dust and what dust or climate factors act as drivers to changes in snowmelt timing. Previous studies have found that end-of-year dust concentration has a strong correlation to change in date of snow disappearance (Skiles et al., 2012; Painter et al., 2015). The underlying motivation for this work is to further our operational understanding of dust- on-snow modifications to snowmelt timing.

## CHAPTER 2. RESEARCH INVESTIGATION

### **2.1. Introduction**

#### *2.1.1. Background*

Solar radiation provides most of the energy for melt in continental mountain snowpack (Bales et al., 2006; Painter et al., 2007). Airborne desert dust deposited on Colorado snowpack reduces surface albedo (Lawrence et al., 2010; Deems et al., 2013), altering the snowpack energy balance and accelerating the timing of snowmelt by 18 to 51 days (Painter et al., 2007; Skiles et al., 2012). Current National Weather Service (NWS) Upper Colorado River Basin streamflow forecasting is based on a coupled temperature-index snowmelt model (SNOW-17; Anderson, 1976) and soil moisture model (Sac-SMA; Burnash et al., 1973). Temperature-index models have a limited ability to account for the radiation components of continental mountain snowpack energy balance (Franz et al., 2008; Follum et al., 2019). The combination of dust loading with variations in magnitude of SWE and meteorological factors each season modifies snowpack energy balance and introduces variations in melt timing (Deems et al., 2013; Painter et al., 2017). These variations may cause considerable uncertainty in operational streamflow forecasting (Bryant et al., 2013). We present patterns of dust loading and snowpack energy absorption over 13 years to better characterize the magnitude of dust influence on snowmelt timing.

#### *2.1.2. Research Objectives*

We determine the patterns of additional snowpack energy absorption and snow melt acceleration due to dust at a small study basin in the San Juan Mountains over 13

years. The first objective is to quantify dust-enhanced energy absorption for each year and determine the relative influence of certain dust and meteorological variables on altering snowpack energy balance. The second objective is to find the difference in snow cover duration between actual (dusty) and simulated ideal (clean) snowpack to characterize the shifts in melt timing for each year. The third objective is to compare differences in melt timing to dust loading, snow characteristics and meteorological variables to assess potential drivers of interannual patterns in snow melt acceleration.

## **2.2. Study Site and Datasets**

### *2.2.1. Study Basin and Automated Data*

We examined dust and snowpack characteristics over 13 years (WY2007 through 2019) at a study site in the San Juan Mountains of southwestern Colorado. Senator Beck Study Basin (SBB) is a 2.91km<sup>2</sup> continental high-elevation (3362 to 4118 m) research watershed that sits at the headwaters of the Uncompahgre River (Figure 1) in the Upper Colorado River Basin (UCRB).

Two micrometeorological towers measure data including radiation fluxes and energy balance summarized in 1-hour, 3-hour, and 24-hour arrays, with a period of record from 2005 to present. The towers are located at 3371 m (Swamp Angel Study Plot, SASP) and 3714 m (Senator Beck Study Plot, SBSP) representing the two principal terrains of the study basin (subalpine forest and alpine tundra, respectively) (Landry et al., 2014). Manual snow profile assessments are collected at both sites approximately weekly during ablation within an undisturbed study plot directly alongside each automated tower, and those measurements are archived by the Center for Snow and Avalanche Studies (CSAS) <[snowstudies.org](http://snowstudies.org)>.

### *2.2.2. Snowpack Development and Dust Timing*

Peak SWE for WY2007 to 2019 at SASP ranged from 543mm (WY2018) to 936mm (WY2011) with an average peak SWE of 719mm. The average date of peak SWE for the period was 13 April, with earliest peak SWE occurring on 18 March in WY2012 and latest peak SWE on 1 May in both WY2011 and WY2019 (Figure 2A). Date of peak SWE for each individual WY are the defining thresholds to characterize dust events as “pre-peak” or “post-peak” (Figure 3). The timing of dust deposition during snowpack development is connected to potential dust-enhanced energy absorption, as the nominal depth of shortwave radiation penetration into the snowpack is around 30cm (Painter et al., 2012). Later-season events can remain closer to the snow surface and have an earlier effect on snow albedo. The timing and magnitude of seasonal snowpack deposition are fundamentally connected to melt timing and magnitude.

### *2.2.3. CSAS Snow Stake Data*

Snow accumulation, wind redistribution, and heterogeneous snowmelt can change the gradient of the snow surface around the towers (Painter et al., 2012). Therefore, assuming a level snow surface and calculating snow albedo with uncorrected visible irradiance can be erroneous. To estimate the local slope and aspect of the changing snow surface, CSAS staff manually recorded snow depths from the snow stake arrays at both SA and SB from WY2006 to WY2012. The subalpine site had four stakes arranged around the central tower whereas the alpine site had six stakes due to greater snow surface variability from stronger wind redistribution (Painter et al., 2012). We determined the plane of best fit to these snow depth arrays to use in combination with seasonal solar position to correct albedo incident angle.

#### 2.2.4. CSAS Snow Pit Data

In addition to the automated continuous micrometeorological tower data, CSAS staff collect approximately weekly manual measurements of snow profile characteristics at both sites. These profile assessments consist of excavating a snow pit to the ground and collecting a temperature profile, describing snowpack stratigraphy (including layer interval, grain shape and size) and liquid water content, and measuring bulk SWE. Bulk snow density is calculated from the depth and SWE measurements. If dust layers are present, dust stratigraphy (depth, number of layers) is measured and dust characteristics (approximate grain size, color) are recorded. CSAS assigns numbers to each perceptible dust layer within the snowpack to allow tracking throughout accumulation and ablation. Bulk dust samples (“all layers merged,” or ALM) are collected towards the end of each snow season.

#### 2.2.5. SNOTEL Site and Data

Daily SWE and snow depth data were retrieved from the Red Mountain Pass (RMP) SNOTEL site from the Natural Resources Conservation Service (NRCS) <[www.nrcs.usda.gov](http://www.nrcs.usda.gov)>. RMP is located approximately 1.8 km SSW of the study basin at 3413 m elevation in a forested clearing with a western aspect. Bulk snow density was calculated at RMP and used to derive daily SWE at SASP from the measured depth, as density has less spatial variation than SWE or snow depth (Elder et al., 1991; López-Moreno et al., 2013).

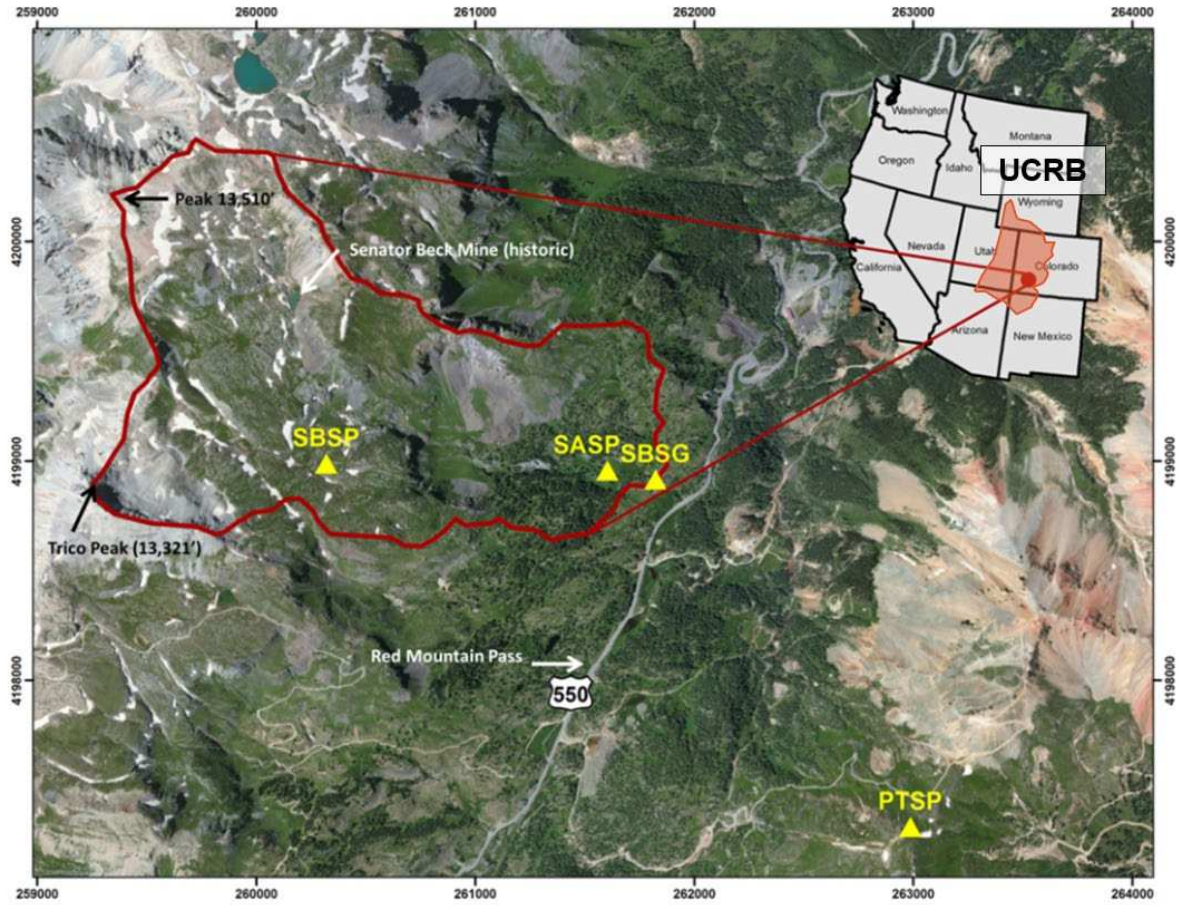


**Figure 1.** Map of study basin within the Upper Colorado River Basin (UCRB). Yellow triangles mark location of meteorological towers SASP (sub-alpine) and SBSP (alpine). Stream gauge (SBSG) and third tower (PTSP) are not referenced in this research (*after Landry et al., 2014*).

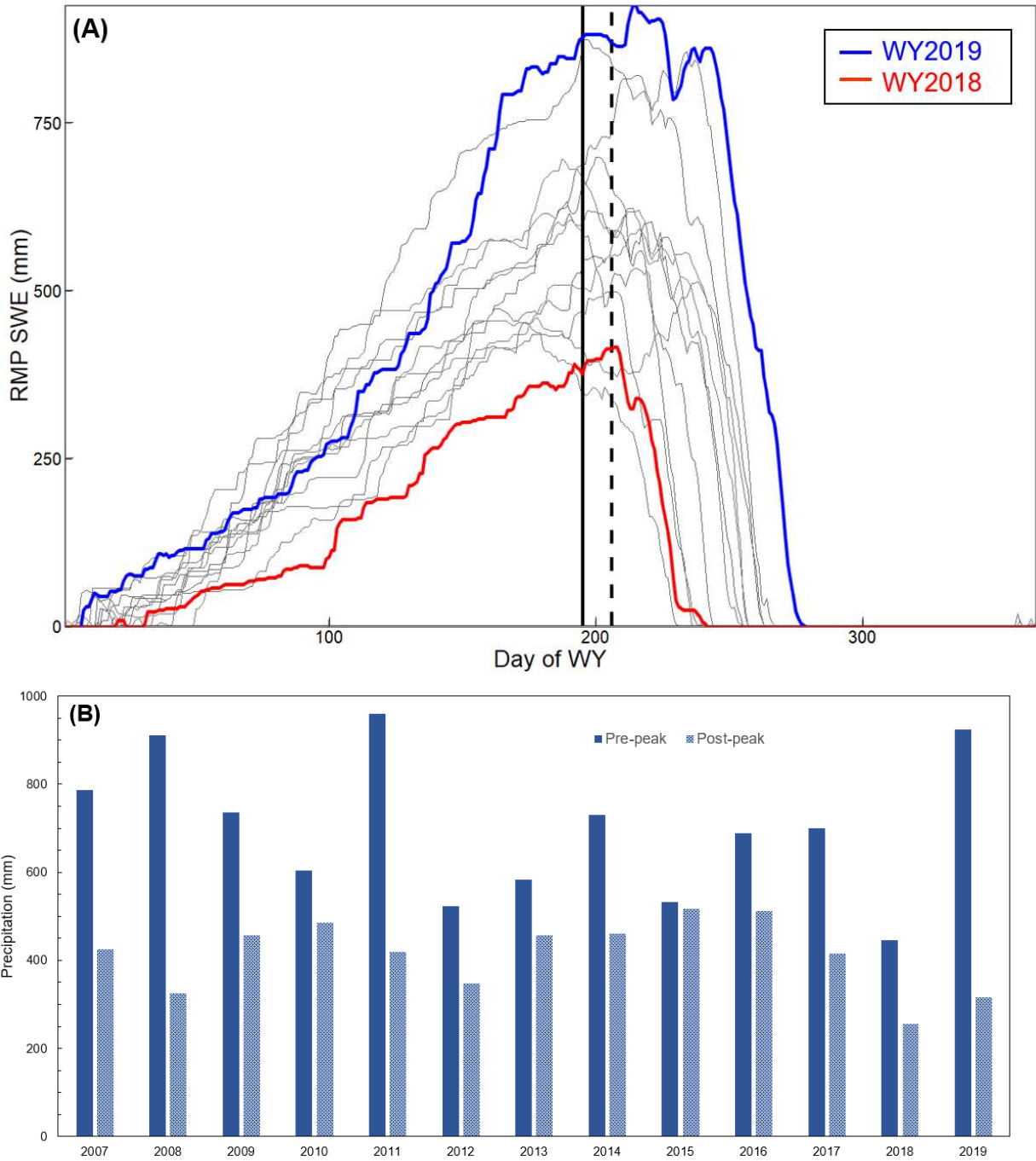


**Figure 2.** Daily SWE from RMP SNOTEL (A) from WY2007 to WY2019. Average date of peak SWE at the station is 25 April (dashed line) whereas at SASP average peak SWE is 13 April (solid line). WY2019 had the maximum peak SWE and WY2018 had the minimum peak SWE for the period of record, all other years are in grey. Precipitation inputs (B) before peak SWE are all larger than inputs after peak SWE for SASP. “Pre-peak” and “post-peak” identification is specific to date of peak SWE for the individual WY, and precipitation is considered over the entire WY.

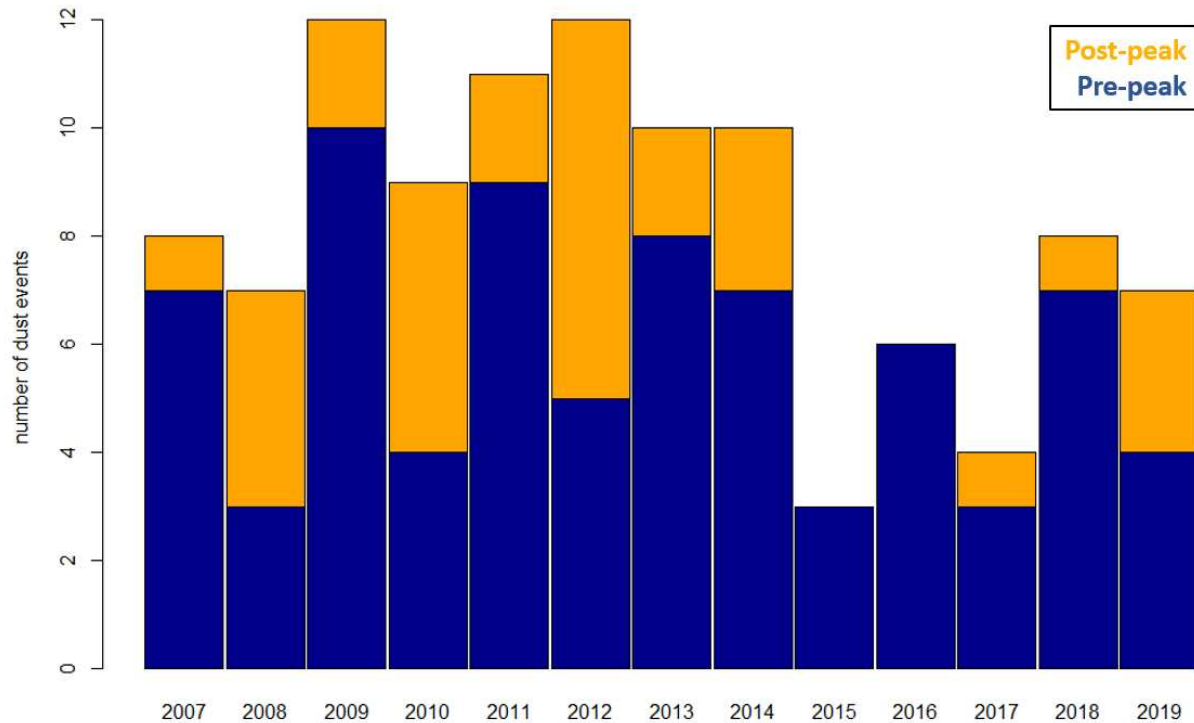


**Figure 3.** Dust events recorded at SASP from WY2007 to 2019. “Pre-peak” and “post-peak” identification is specific to date of peak SWE for the individual WY. Three water years had 50% or more dust events deposit after peak SWE (WY2008, WY2010, and WY2012).

## 2.3. Methods

### 2.3.1 Albedo Corrections

Calculating snow albedo with uncorrected radiation flux measurements assumes a level snow surface, which can be erroneous given wind redistribution, snow accumulation patterns, and heterogenous snowmelt (Painter et al., 2012). We retrieved the slope and aspect of the snow surface from snow stake array observations. The time series of slope and aspect was linearly interpolated between each weekly set of measurements to approximate a daily snow surface. In addition to the geometric correction of non-level snow surface, we corrected for seasonally shifting solar position.

Geometric and solar position adjustments are combined with the following relation (after Painter et al., 2012):

$$\cos \beta = \cos \theta_s \cos \theta_n + \sin \theta_s \sin \theta_n \cos \{\Phi_s - \Phi_n\} \quad (\text{Equation 1})$$

where  $\beta$  is the local solar zenith angle,  $\theta_s$  is the solar zenith angle for the horizontal surface,  $\Phi_s$  is the solar azimuth angle,  $\theta_n$  is the surface slope, and  $\Phi_n$  is the surface aspect. The scalar ( $M_\beta$ ) by which we corrected measured hourly downward shortwave radiation flux (irradiance) values to at-surface irradiances is (after Painter et al., 2007):

$$M_\beta = \frac{\cos(\beta)}{\cos(\theta_s)} \quad (\text{Equation 2})$$

Snow surface albedo was calculated from the corrected irradiance and observed reflected flux (Figure 4).

Snow stake array depth observations were only collected for WY2007-2012, so the mean slope and aspect for each calendar day were used to approximate a daily corrective  $M_\beta$  value for WY2013-2019 (Figure 5).

In addition to correcting for non-level snow surface, we also adjusted for snow deposition on the up-facing pyranometers. Accumulation on the up-facing pyranometers reduces the measured incoming irradiance compared to the actual incoming amount. The alpine site has a more continuous record of irradiance since it experiences higher windspeeds which regularly clear the snow off of the up-facing pyranometers (Landry et al., 2014). We used the alpine albedo to retrieve the sub-alpine irradiance as follows:

$$\text{Irradiance (sub-alpine)} = \frac{\text{Reflected flux (sub-alpine)}}{\alpha (\text{alpine})} \quad (\text{Equation 3})$$

### 2.3.2. Dust Concentrations

Total dust concentrations were determined from the ALM samples collected towards the end of each ablation season. Bulk samples were processed by the U.S. Geological Survey of Colorado to yield dust loading and geochemical properties (Reynolds et al., 2020). Dust loading ( $\text{g m}^{-2}$ ) was transformed to end-of-year dust concentration using the  $3\text{cm} \times 0.5\text{m}^2$  sample volume and the bulk snow density observed on the collection date.

### 2.3.3. Absorbed Energy Calculations

We calculated the dust-enhanced energy absorption (DEAE) based on snow surface albedo within visible wavelengths. There is an indirect effect from LAPs of increased snow albedo due to larger snow grain size from acceleration of grain growth and the earlier exposure of darker substrate (Hansen and Nazarenko, 2004) but the greater divergence of LAP-influenced snow surface albedo from that of clean snow occurs within the visible spectrum (Melloh et al., 2001; Figure 6).

Surface visible DEAE ( $\text{W m}^{-2}$ ) is calculated after Skiles et al. (2012) as

$$\text{DEAE}_{VIS} = E_{VIS} \Delta_{VIS} \quad (\text{Equation 4})$$

where  $E_{VIS}$  is the visible irradiance determined from the difference between broadband and NIR/SWIR irradiances and  $\Delta_{VIS} = 0.92 - \alpha_{VIS}$  ( $\alpha_{VIS}$  is calculated visible albedo from tower measurements and 0.92 is the observed visible albedo for dust-free snow at the study site). Previous studies also calculated the additional NIR/SWIR energy absorption due to dust based on an empirical relation to grain coarsening in the absence of dust developed with two years of dust and snow observations in the study basin (Painter et al., 2007). The total energy absorbed from the combined direct visible effect and indirect

NIR/SWIR effect was identified as “dust radiative forcing” (e.g., Painter et al., 2007; Skiles et al., 2012; Skiles et al., 2015).

Daily mean visible DEAE is calculated from 1 April to observed SAG for each year, and “springtime” irradiance and precipitation are totaled over the same interval. While dust-enhanced energy absorption may begin earlier in the season, this period captures typical snowpack ablation from peak SWE to complete melt-out when DEAE has the greatest effect on melt timing.

#### *2.3.4. Snow Energy Balance Model*

We used the point-based snow energy balance SNOBAL to model hypothetical snowpack at the sub-alpine site under actual hourly conditions (“dusty”) and snowpack with the dust effect removed (“clean”) to understand differences in melt timing. SNOBAL approximates the snowpack as two layers: the upper 25cm layer exchanges energy with the atmosphere, and the underlying remainder of the snowpack acts as an energy and mass storage layer (Figure 7) (Marks and Dozier, 1992; Marks et al., 1992). We ran the model over spring melt season at the sub-alpine site using data from manual snow assessments and automated tower collection. The starting snow conditions of each model run were determined from the field measurements collected closest in time to 13 April (average date of peak SWE for the study plot). The model calculated hourly changes in snow state variables using observed hourly forcing variables (Table 1) and precipitation inputs.

**Table 1.** Predicted state variables and required forcing variables for SNOBAL (after Marks et al., 1998)

<b>State Variables</b>	<b>Forcing Variables</b>
Snow depth (m)	Net solar radiation ( $W\ m^{-2}$ )
Snow density ( $kg\ m^{-3}$ )	Incoming longwave radiation ( $W\ m^{-2}$ )
Snow surface layer temperature ( $^{\circ}C$ )	Air temperature ( $^{\circ}C$ )
Average total snowpack temperature ( $^{\circ}C$ )	Vapor pressure (Pa)
Average snow liquid water content (%)	Wind speed ( $m\ s^{-1}$ )

“Dusty” model runs were completed with actual recorded conditions. “Clean” model runs modified the hourly net solar radiation inputs by removing the DEAE. For all runs, total precipitation mass recorded by an electronic weighing gauge at the sub-alpine site was partitioned into rain or snow based on dewpoint temperature. Percentage of precipitation falling as snow and fresh snow density were assigned according to Table 2.

**Table 2.** Precipitation partitioning table based on dewpoint temperature (after Susong et al., 1999)

<b>Temperature (<math>^{\circ}C</math>)</b>	<b>Percent Snow</b>	<b>Snow density (<math>kg\ m^{-3}</math>)</b>
$T < -5$	100	75
$-5 \leq T < -3$	100	100
$-3 \leq T < -1.5$	100	150
$-1.5 \leq T < -0.5$	100	175
$-0.5 \leq T < 0$	75	200
$0 \leq T < 0.5$	25	250
$0.5 \leq T$	0	0

All model runs set soil temperature to  $0^{\circ}C$  since soil temperatures are generally approximately  $0^{\circ}C$  at time of peak snow accumulation and are considered to have a relatively negligible contribution to snowpack energy balance (Marks and Dozier, 1992). Snow surface aerodynamic roughness ( $z_0$ ) was set to 0.001 meters (Fassnacht, 2004)

for all model runs based on the determination of Skiles et al. (2012) which found the model results not highly sensitive to reasonable  $z_0$  values ( $< 0.005\text{m}$ ).

The accuracy of modeled SWE was assessed by comparing “dusty” SWE to two observations of SWE: derived and manually measured. Derived SWE is a combination of the calculated daily bulk snow density at Red Mountain Pass SNOTEL and the observed daily snow depth at the study site. The manual measurements of SWE were collected on an approximately weekly basis by CSAS staff during snow pit assessments.

The difference in melt-out dates ( $\Delta\text{SAG}$ ) between the modeled “dusty” scenario and the modeled “clean” scenario is a measure of melt acceleration due to amount of dust-enhanced absorbed visible energy (DEAE), since the two scenarios are otherwise modeled with identical snow state variables and meteorological inputs.

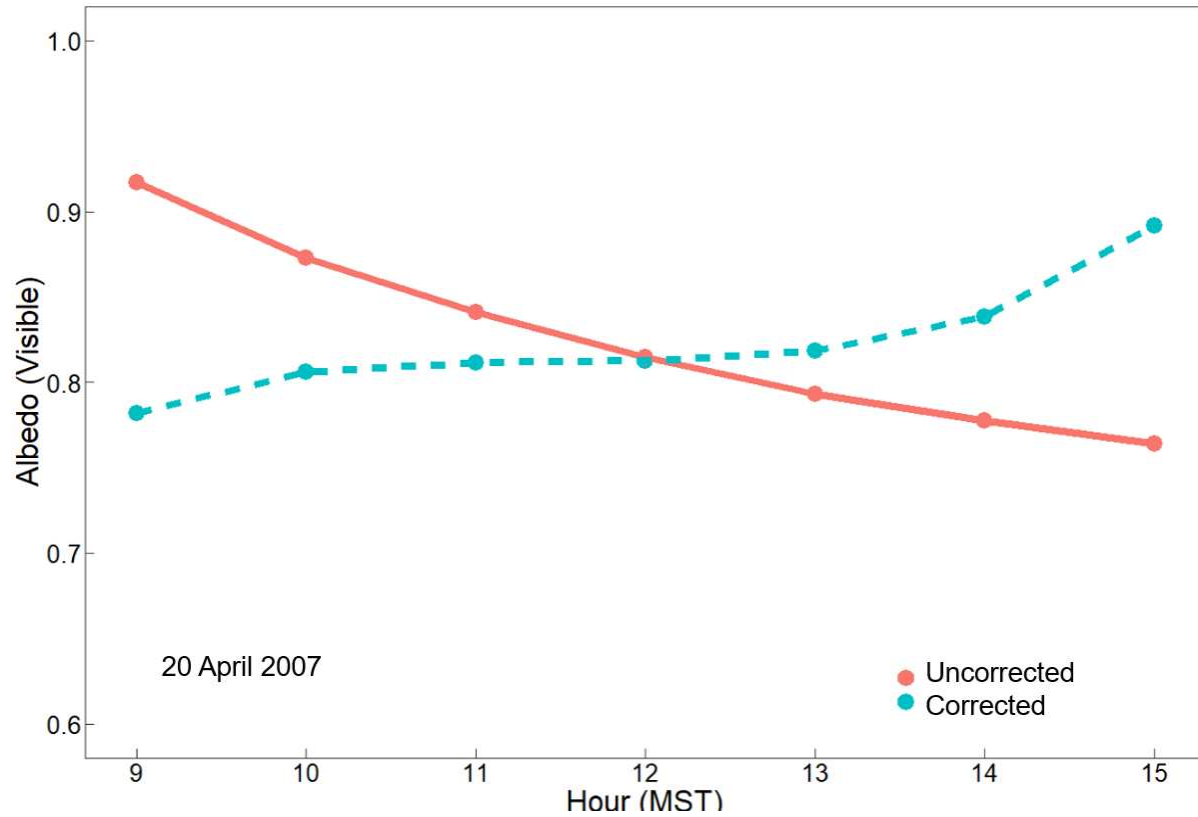


**Figure 4.** Hourly snow surface albedo was corrected for a non-level snow surface and seasonally shifting solar position to capture diurnal variation.

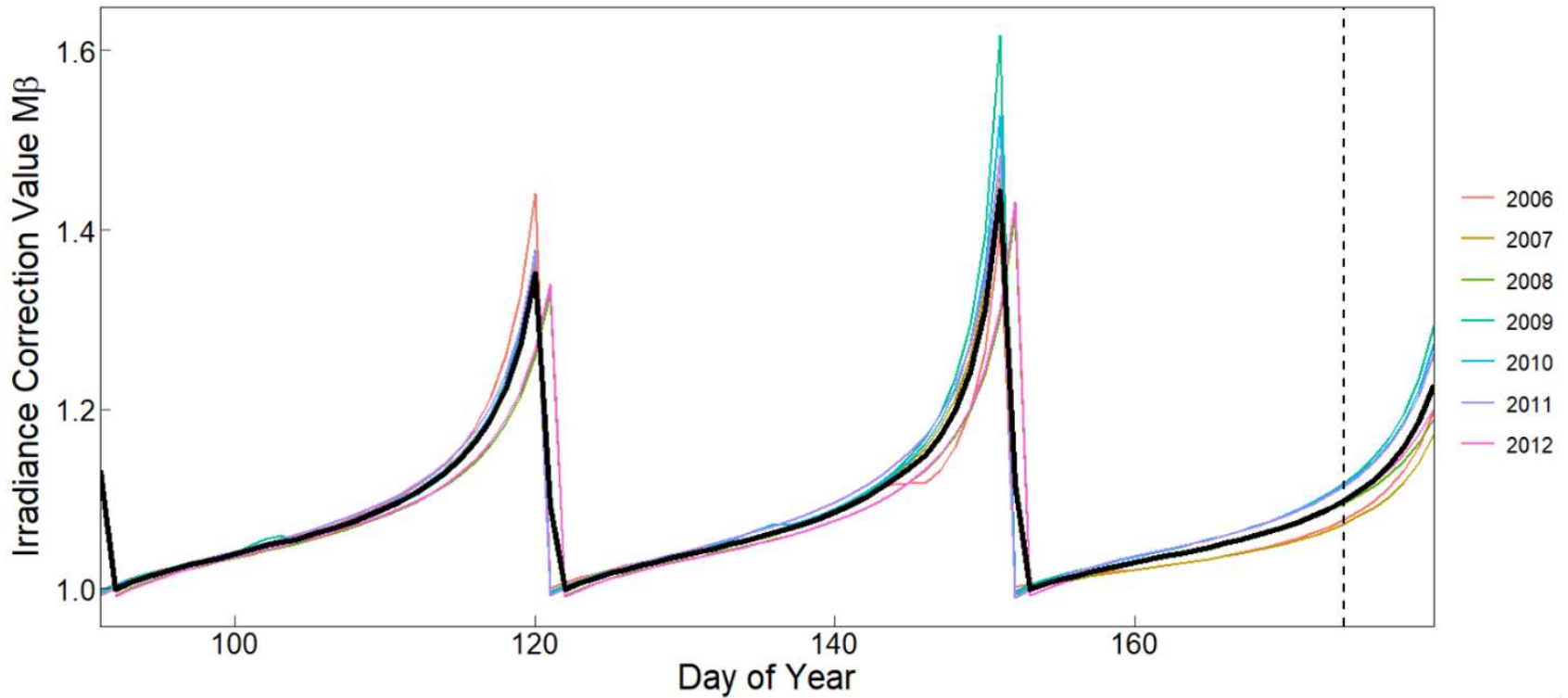


**Figure 5.** Observed snow surface correction values for WY2007-2012 (color lines) and approximated surface correction value used for WY2013-2019 (black line) over ablation season (April, May, and June). Vertical dashed line is the latest observed date of SAG (WY2011) for the period.

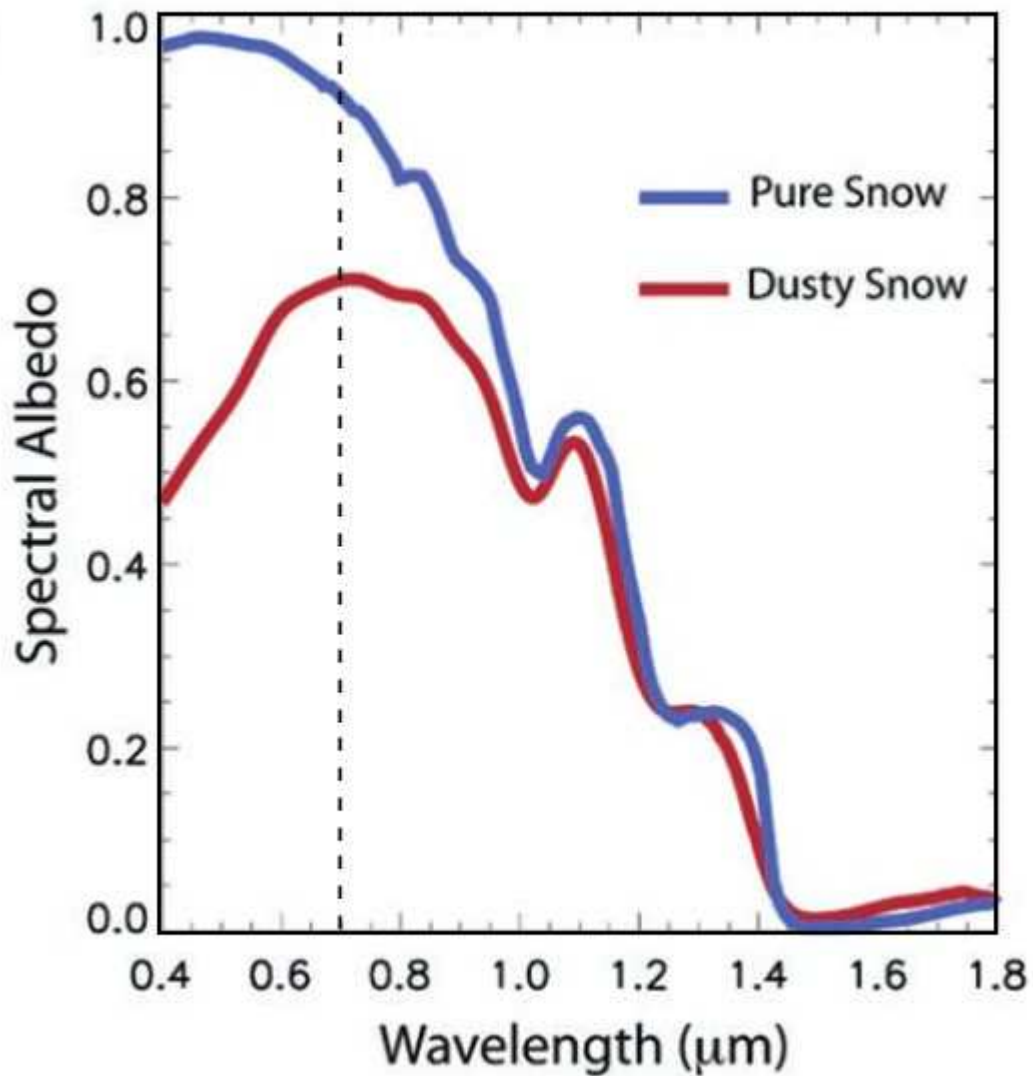


**Figure 6.** Comparison of albedo between clean snow (modeled) and dusty snow (measured, dust concentration =  $0.37 \text{ mg g}^{-1}$ ) with vertical line at the  $0.7\mu\text{m}$  transition from visible spectra to near-infrared/shortwave-infrared spectra (after Painter et al., 2012).

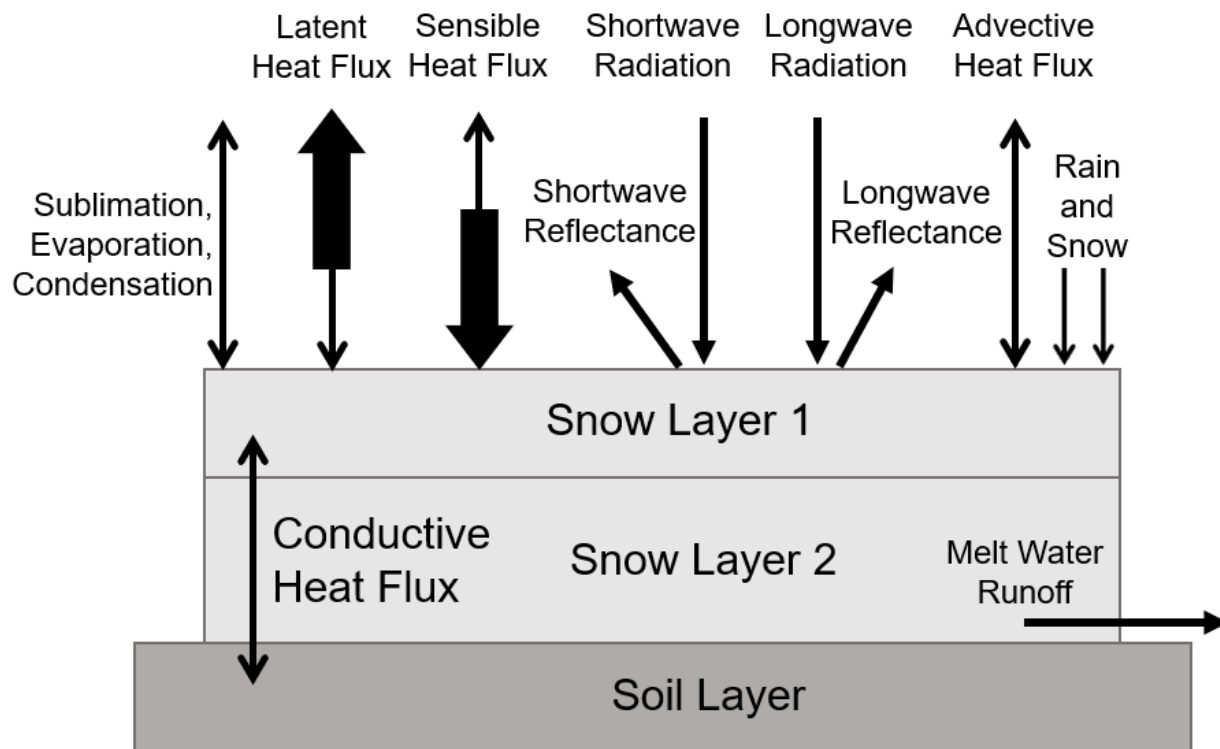


**Figure 7.** Conceptual diagram of SNOBAL inputs and internal processes (*after Marks et al., 1998*).

## 2.4. Results

### 2.4.1. Daily Mean Visible DEAE

For WY2007 to WY2019, daily mean visible DEAE during ablation ranged from  $31 \text{ W m}^{-2}$  (WY2015) to  $50 \text{ W m}^{-2}$  (WY2019). Cumulative daily mean visible DEAE typically did not exceed  $3000 \text{ W m}^{-2}$  while snow was present (Figure 8). The outlier is WY2019 which had snowpack persist for 33 days longer than the next-latest observed SAG (WY2011). These additional days of snowpack persistence result in the longest period over which DEAE is cumulated and also occur at the end of ablation season as

the amount of incoming solar radiation is increasing. The combination of these two effects results in a high average daily DEAE which is an outlier representation of dust-affected snow dynamics. In comparison, WY2015 had the lowest daily mean visible DEAE due to a combination of shorter snow cover duration and dust-on-snow system dynamics during ablation. Several late-spring snowfall events in April and May of 2015 temporarily increased snow surface albedo (Figure 9) which in turn decreased visible DEAE after each event and drove the springtime daily mean visible DEAE lower. Seasonal average values of DEAE are the result of complex daily dynamics.

Approximated snow surface correction values (Equation 2) were assessed by comparing the resulting scaled incoming visible irradiance to incoming visible irradiance scaled with observed snow surface conditions. The average difference between observed irradiance values and approximated values over the whole snow season for WY2007 to WY2012 was small ( $-0.04 \text{ W m}^{-2}$ ). However, comparison of observed to predicted irradiance had an RMSE of  $8 \text{ W m}^{-2}$  during ablation for WY2007 to WY2012.

#### *2.4.2. DEAE and Potential Drivers*

Dust concentration and daily mean visible DEAE have no significant correlation for all years and a strong logarithmic correlation when the outlier and WY2008, WY2014, and WY2017 are excluded (Table 3). The dust distribution has two modes: low-dust years (2007, 2008, 2011, 2012, 2014-2018) have end-of-year dust concentrations below  $2 \text{ mg g}^{-1}$  and high-dust years (2009, 2010, 2013) have concentrations above  $4 \text{ mg g}^{-1}$  (Figure 10A). Additionally, the range in daily mean visible DEAE is  $8 \text{ W m}^{-2}$  for low-dust years and  $2 \text{ W m}^{-2}$  for high-dust years. The logarithmic

increase of DEAE is likely based on the nonlinear optical response of albedo reduction to increases in dust concentration (Skiles et al., 2012).

Number of dust events and daily mean visible DEAE (Figure 10B) have no significant correlation for all years and a weak linear correlation when the outlier is excluded (Table 3). Number of dust events has been previously determined to be a poor predictor of near-surface albedo or of seasonal DEAE (Painter et al., 2012) without additional knowledge of dust layer burial depth and relative amount of irradiance.

Cumulative springtime irradiance and daily mean visible DEAE have no correlation for all years (Table 3). When the outlier is excluded, two potentially distinct linear groups are apparent (Figure 10C). WY2007, WY2012, WY2015, and WY2018 form one group with strong linear correlation to irradiance ( $R^2 = 0.98$ ). The second group (all other WYs) is also linearly correlated to irradiance ( $R^2 = 0.67$ ). Both groups have a negative relation of daily mean visible DEAE to cumulative springtime irradiance.

Cumulative springtime precipitation and daily mean visible DEAE have no correlation for all years (Table 3). A negative linear correlation is evident when the outlier and WY2011, WY2012, and WY2018 are excluded (Figure 10D). Springtime precipitation that accumulates as snow increases the surface albedo and leads to decreased DEAE.

**Table 3.** Correlations of daily mean DEAE with dust and climate variables

<b>Variable</b>	<b><math>R^2</math> (all years)</b>	<b><math>p</math> Value</b>	<b><math>R^2</math> (some years excluded)</b>	<b><math>p</math> Value</b>
End-of-year dust concentration	0.21	0.116	0.86 (logarithmic)	$p < 0.001$
Total number of dust events	0.15	0.198	0.31 (linear)	0.059
Cumulative irradiance	0.03	0.597	0.98 and 0.67 (linear, two groups)	0.008 and 0.013
Cumulative precipitation	0.02	0.653	0.63 (linear)	0.011

#### 2.4.3. Modeled SWE and Snow Cover Duration

Overall, SNOBAL simulated observed SWE well (Table 4). The difference between modeled and derived SWE is 34mm greater than between modeled and manually measured SWE. Typically, model comparisons are poorer for shorter timesteps than for longer timesteps (Moriasi et al., 2007) so this performance difference between derived SWE (daily timestep) and manually measured SWE (weekly timestep) is unsurprising.

**Table 4.** Two evaluations of SNOBAL model SWE to two empirical SWE measurements (see Appendix B for individual WY results).

<b>SWE measurement</b>	<b>RMSE (mm)</b>	<b>NSE</b>
Derived SWE (SNOTEL + CSAS)	119	0.81
Manual Snow Pit SWE (CSAS)	85	0.83

Modeled “clean” snowpack has slower melt rates than modeled “dusty” snowpack, which has rates similar to observed melt rates (Figure 11). Some divergence between modeled and observed SWE is more apparent in years with late-season precipitation events (e.g., WY2013 and WY2016). For all years, derived SWE is consistently lower than manually measured SWE at the snow pits (average difference of 93mm). Higher SWE and later observed complete melt-out (e.g., WY2007 and WY2014) occur in the snow pit plot.

For 11 of the 13 WYs, modeled dusty SAG was less than 2 days different than observed SAG. The two outliers were WY2016 and WY2019 which modeled melt-out 2 and 31 days earlier than observed, respectively (Figure 11). The greatest degree of melt acceleration due to dust was in WY2009 (31 days earlier) and the least melt acceleration was in WY2015 (11 days earlier).

#### *2.4.4. Snow Cover Duration and Potential Drivers*

Dust concentration and  $\Delta$ SAG (Figure 12A) have a weak logarithmic correlation for all years and a stronger logarithmic correlation when the outliers and WY2013 and WY2012 are not considered (Table 5). When dust concentrations range from 0 to 2 mg g<sup>-1</sup> the  $\Delta$ SAG increases rapidly for small increases in dust concentration (range of 16 days difference from WY2015 to WY2011). As dust concentrations increase above 2 mg g<sup>-1</sup> the corresponding increase in  $\Delta$ SAG is less rapid (range of 4 days difference from WY2011 to WY2009). This emphasizes that even small dust concentrations can be correlated to shifts in snow cover duration.

The number of dust events and  $\Delta$ SAG (Figure 12B) have a weak correlation for all years and a strong positive linear correlation when outliers and WY2012, WY2013,

and WY2018 are not considered (Table 5). Years when many dust events occurred can have a large shift in snow cover duration, however this relation may be misleading given the influences of relative timing of these events and degree of dust loading.

Cumulative springtime irradiance and  $\Delta$ SAG (Figure 12C) have no significant correlation for all years and a strong positive linear correlation when outliers and WY2009, WY2015, and WY2017 are not considered (Table 5). As snowpack receives more incoming solar radiation, larger shifts in snow cover duration are possible.

Cumulative springtime precipitation and  $\Delta$ SAG (Figure 12D) have no significant correlation for all years and a strong positive linear correlation when outliers and WY2009 and WY2015 are not considered (Table 5).

**Table 5.** Correlations of  $\Delta$ SAG with dust and climate variables

<b>Variable</b>	<b><math>R^2</math> (all years)</b>	<b><math>p</math> Value</b>	<b><math>R^2</math> (some years excluded)</b>	<b><math>p</math> Value</b>
End-of-year dust concentration	0.30	0.052	0.61 (logarithmic)	0.013
Total number of dust events	0.29	0.055	0.92 (linear)	$p < 0.001$
Cumulative irradiance	0.08	0.337	0.82 (linear)	0.002
Cumulative precipitation	0.13	0.227	0.65 (linear)	0.015

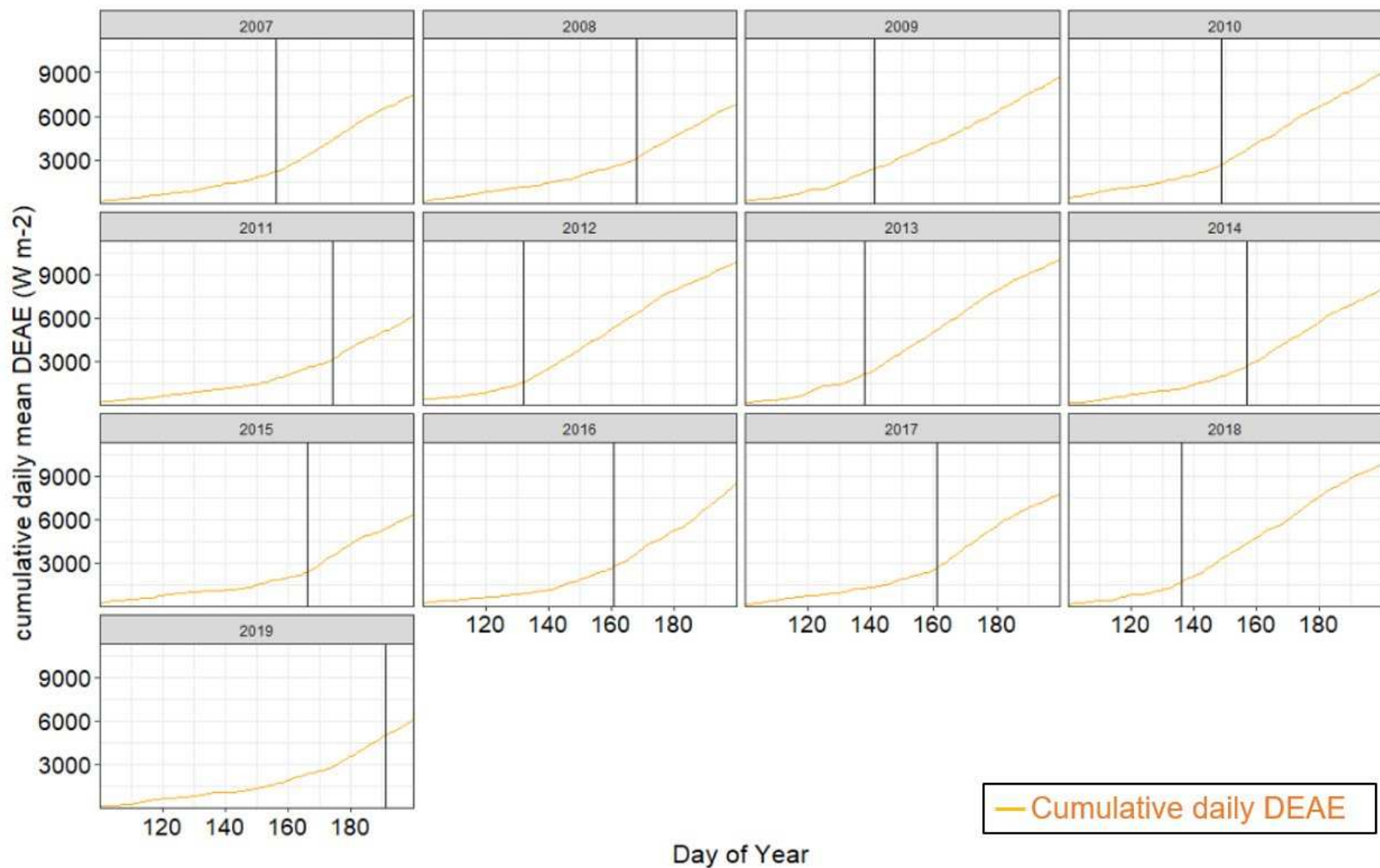


**Figure 8.** Cumulative daily mean DEAE for WY2007 to WY2019. Vertical black lines are the observed date of SAG for each WY. Daily mean absorbed energy values after these dates are due to the lower albedo of the ground surface and are not necessarily dust-enhanced.

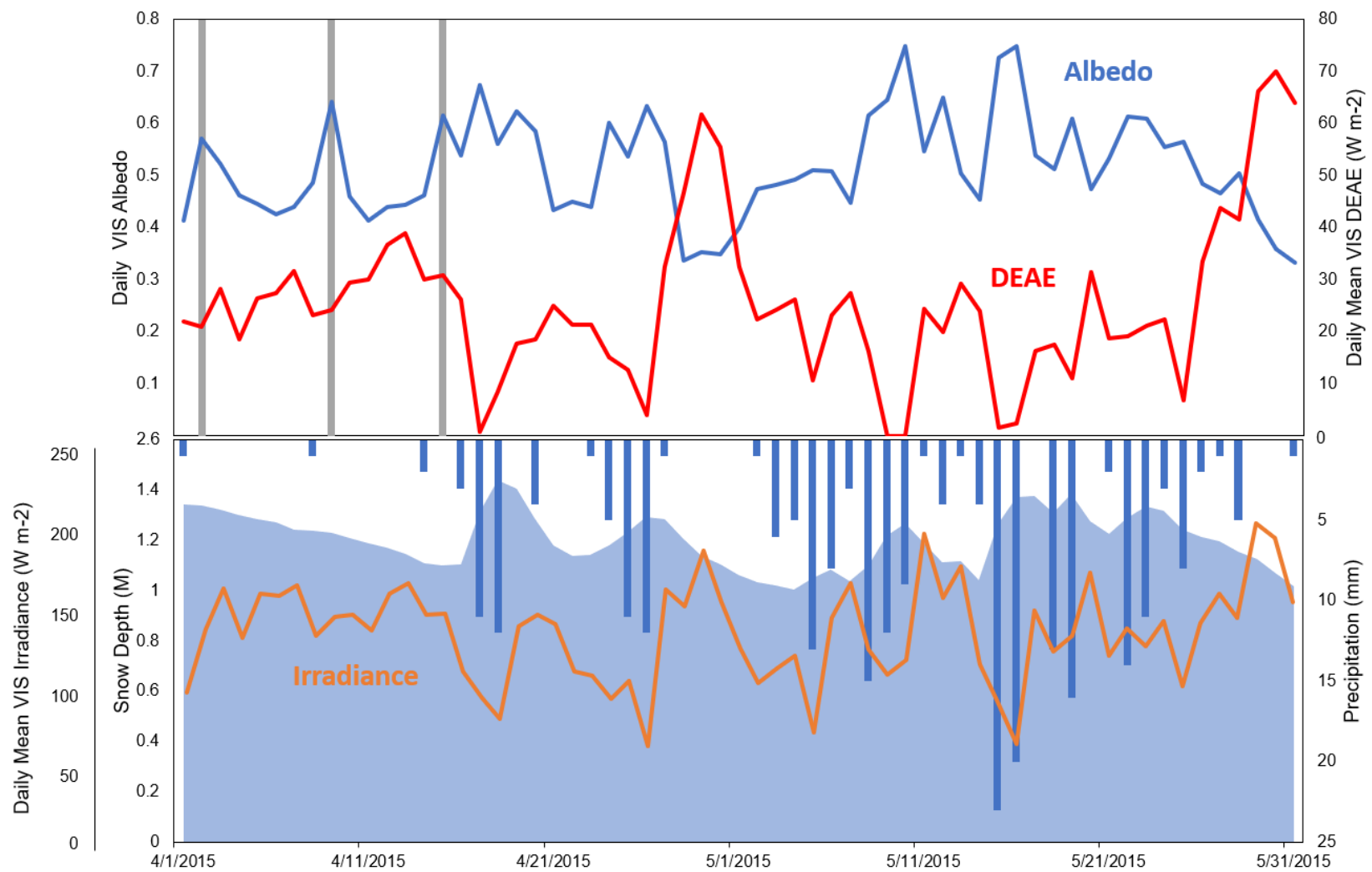


**Figure 9.** Snow surface albedo and daily mean visible DEAE (above) compared to snow depth, precipitation inputs, and visible irradiance (below) for April and May of WY2015. Vertical grey bars represent dust events. WY2015 was a low-dust year ( $0.51 \text{ mg g}^{-1}$  end-of-year dust concentration) with the smallest  $\Delta\text{SAG}$  (11 days).

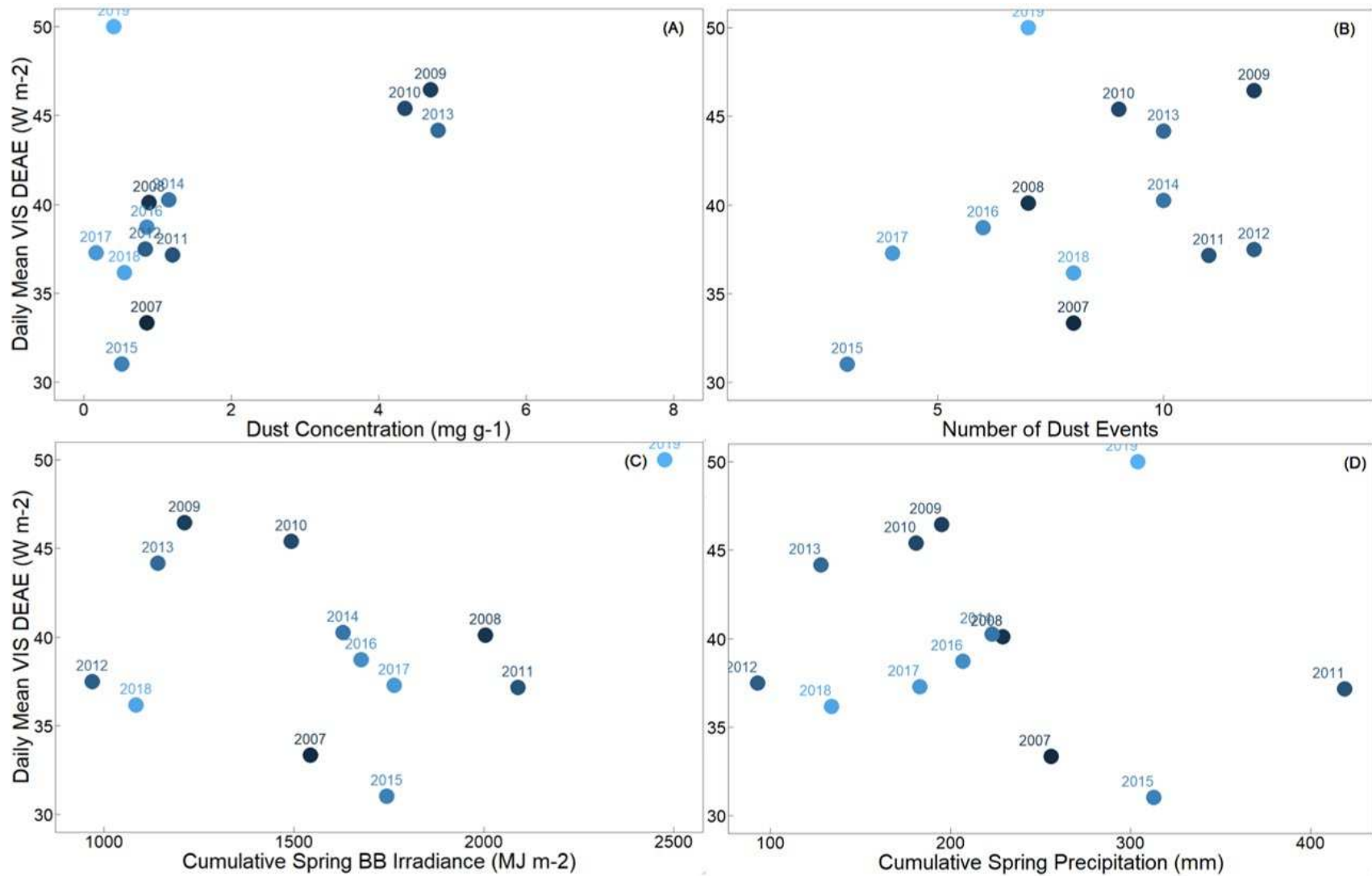


**Figure 10.** Daily mean visible DEAE compared to end-of-year dust concentration (A), number of dust events (B), cumulative spring broadband irradiance (C), and cumulative spring precipitation (D).

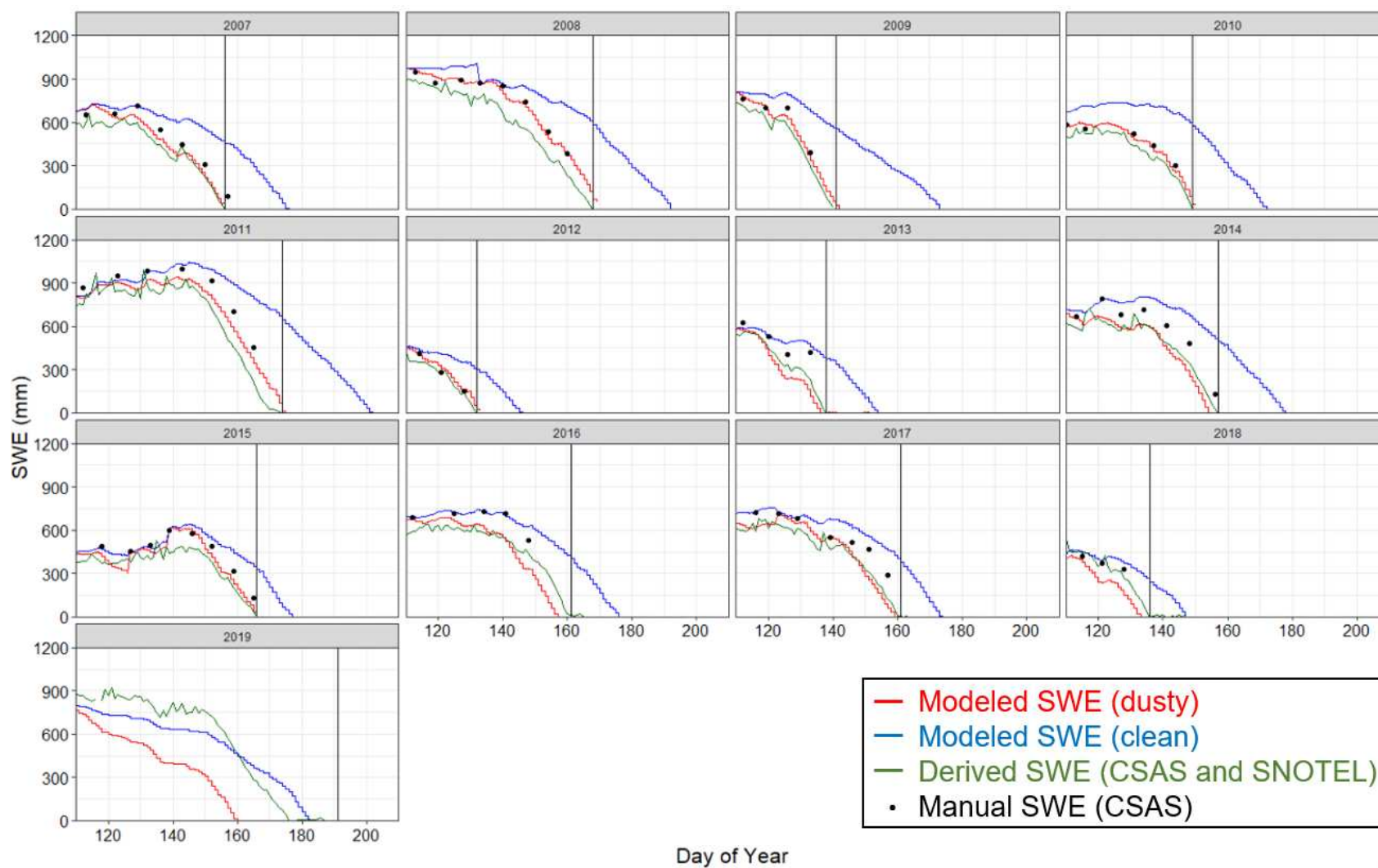


**Figure 11.** Modeled SWE curves and observed SWE curves for WY2007 to WY2019. “Derived” SWE is calculated from observed snow density at Red Mountain Pass SNOTEL and observed snow depth at CSAS study plot. Vertical black lines indicate date of observed SAG for each year. The red line (modeled SWE under actual conditions) matches the seasonal patterns of manually measured bulk SWE (black points) fairly well, in particular capturing late-season melt rates.

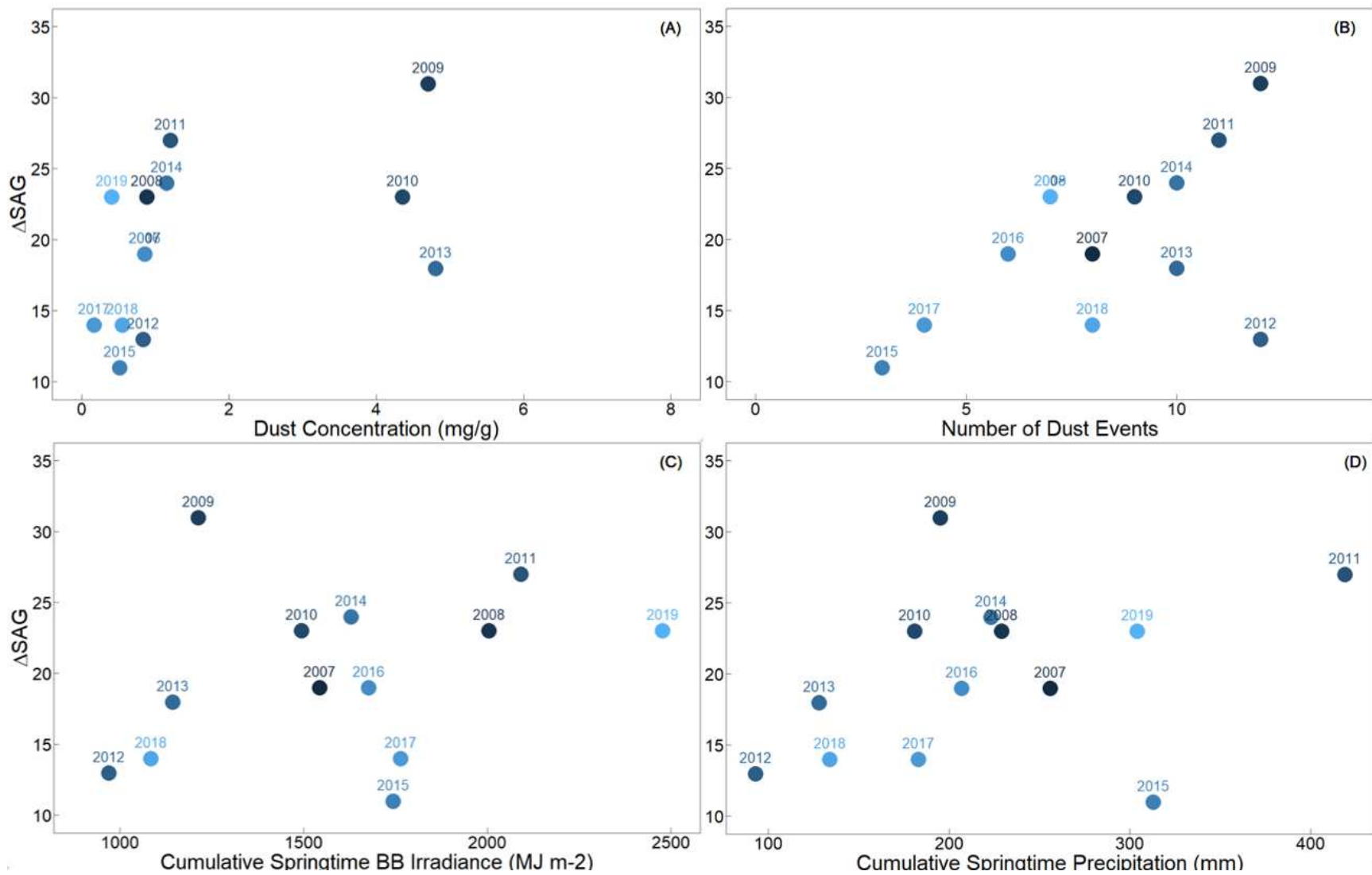


**Figure 12.** Difference in snow cover duration ( $\Delta SAG$ ) compared to end-of-year dust concentration (A), number of dust events (B), and cumulative springtime irradiance (C) and precipitation (D).

## 2.5. Discussion

### 2.5.1. DEAE Calculations

DEAE calculations for all years relied on a snow surface correction to albedo which was observed for WY2007 to 2012 and approximated for WY2013 to 2019. Generally, the incoming visible irradiance calculated with the approximated snow surface correction compared well to the irradiance calculated with the observed correction (RMSE of  $8 \text{ W m}^{-2}$ ). The greatest residual was in May of WY2008 which had high SWE and above-average spring windspeeds creating a complex snow surface not fully represented by the approximated value (Figure 4). We investigated the effect of under-estimation and over-estimation of irradiance on a high-dust year (WY2013) and found that daily mean visible DEAE could range from  $39.5$  to  $45.5 \text{ W m}^{-2}$ . A similar investigation of a low-dust year (WY2017) found a range from  $32.5$  to  $38 \text{ W m}^{-2}$ . Despite the potential scale of uncertainty for daily mean visible DEAE calculations for WY2013 to WY2019, the overall pattern of DEAE response to increases in dust concentration would remain a logarithmic correlation.

The scale of our DEAE calculations compares well to previous findings over the general UCRB region. Remote sensing of particulate-enhanced energy absorption from four days in WY2011 over the Uncompaghre Basin found the average instantaneous pixel value ranged from about  $50 \text{ W m}^{-2}$  in mid-May to  $200 \text{ W m}^{-2}$  in mid-June (Seidel et al., 2016). This range is likely in part due to their inclusion of all light-absorbing impurities, assumption of homogeneous snow grain size, and spatial variability due to resolution ( $13.8 \text{ m}$  pixel size). We found hourly visible DEAE to range up to  $234 \text{ W m}^{-2}$  during June of WY2011. Additionally, Bryant et al. (2013) retrieved daily mean radiative

forcing from dust in the visible spectrum only and found a range from 20 to 80 W m<sup>-2</sup> (over WY2000 to WY2010). Our point-based study falls within the observed range of particulate-enhanced energy absorption for the general study area.

The pattern of our daily mean DEAE calculations compares well to previous in-situ studies. Skiles et al. (2015) considered the combined amount of dust-enhanced absorbed energy in both the visible and NIR/SWIR spectra at the same study site from 2005 to 2013. They found a range of daily mean dust-enhanced radiative forcing from 35 W m<sup>-2</sup> (WY2005) to 75 W m<sup>-2</sup> (WY2009). Those daily mean values consider the surface-darkening effect of deposited dust in combination with dust-modified snow grain growth. The combined mean daily energy absorption of surface and grain metamorphism effects has been shown to be on average 25 W m<sup>-2</sup> higher than energy absorption in the visible part of the spectrum alone based on a comparison of two modeled scenarios (Skiles et al., 2015; Skiles, 2014). Additionally, Skiles and Painter (2017) found broadband snow albedo to be controlled by the visible effect of LAPs during the highest dust-loading year on record (WY2013). Broadband albedo (280 to 2800 nm) combines the reflectivity of both visible (400 to 700 nm) and NIR/SWIR (700 to 2500 nm) wavelengths, reinforcing that visible albedo of dust-affected snow can decrease by greater magnitude than NIR/SWIR albedo (Figure 6) and thus drive energy absorption. Despite differences in magnitude of daily mean DEAE, our values follow the same pattern with respect to dust concentration increases as that observed by Skiles et al. (2012) for WY2007 to WY2010 and by Skiles et al. (2015) for WY2010 to WY2013 (Figure 10A).

### 2.5.2. *Potential Drivers of DEAE*

We compared four independent variables to daily mean visible DEAE in a series of simple logarithmic or linear regressions. These comparisons had varying degrees of significance ( $p$ -values in Table 3) reflected in our summary of correlations (Section 2.4.2.). One-variable comparisons cannot represent complex natural systems, so these results should be understood as preliminary (for a glimpse of the multiple regression analysis we are currently exploring, see Appendix C). The exclusion of deviant years in these simple regressions could have been prone to “over-fitting” or arbitrary exclusion of data points to increase correlation coefficients. To avoid this, we attempted to exclude the minimum number of deviant years and understood the patterns in Figure 10 to be a guide of correlation but not necessarily of causation.

The dust, snow, and climate variables we examined are bulk approximations of a dynamic system with sub-seasonal variation. Visible DEAE can change hourly according to incoming visible irradiance and snow surface albedo. Visible surface albedo can change sub-daily according to precipitation inputs, timing of dust layer deposition, and subsequent emergence of dust layers during melt. A majority of the dust events from WY2007 to WY2019 occurred prior to peak SWE (Figure 3). Since the depth of light penetration into the snowpack can vary from several to 10s of cm (Thomas, 1963), the deeper burial of dust is a delay in the effect on surface albedo. Dust events that occur after peak SWE can still be buried by spring storms (Figure 2B) which will temporarily increase surface albedo with fresh snow (Figure 9; Figure 13). The daily response of albedo and visible DEAE to changing precipitation inputs, dust burial depths, and incoming visible irradiance is illustrated by examining April and May

of high-dust WY2009 (Figure 13) and low-dust WY2015 (Figure 9). A storm on 25 April 2009 buried dust with concurring snowfall, causing a temporary increase in albedo due to a fresh snow surface, and then the emergence of the deposited dust by 30 April caused surface albedo to decrease until the next snowstorm on 2 May (Figure 13).

Increasing daily mean visible DEAE is logarithmically correlated to increasing dust concentration (Figure 10A). Deposited dust layers can change surface albedo, allowing greater energy absorption. However, this relation is modified by the amount of available irradiance and burial depth of dust layers. WY2008 and WY2017 had above-average irradiance, likely driving the high daily mean visible DEAE for both years. Additionally, the majority of dust events in WY2008 were deposited after peak SWE (Figure 3) with less than 30% of total SWE accumulating at that same time (Figure 2B). The shallow burial of dust layers positions them closer to the snow surface and potentially leads to an earlier start of energy absorption. The burial depth of dust layers is likely also driving the daily mean visible DEAE lower for WY2014, which received the majority of dust before peak SWE (Figure 3). Skiles and Painter (2017) found no significant relation between albedo and dust buried below 6cm from the snow surface, indicating that deeper burial of dust layers will delay their effect on daily mean visible DEAE.

The number of events alone has little correlation to daily mean visible DEAE (Figure 10B) and two additional variables should be considered: dust concentration and depth of burial. Comparison of WY2009 and WY2012 illustrates the importance of considering dust concentration: both years have the highest number of dust events yet WY2012 has only 30% the dust concentration of WY2009 ( $1.35\text{mg g}^{-1}$  compared to

4.55mg g<sup>-1</sup>). The year with higher dust concentration has greater daily mean visible DEAE. Comparison of WY2017 and WY2015 illustrates the importance of considering burial depth of dust layers. Both years had few dust events and low dust concentration, yet WY2015 had lower daily mean visible DEAE. This is likely due to a greater amount of late-season snow accumulation in WY2015 which delayed dust emergence at the snow surface (Figure 2B).

Greater cumulative springtime irradiance is correlated to lower daily mean visible DEAE (Figure 10C). Closer examination of two distinct groups of points indicate that the negative correlation is likely due to the effect of dust concentration on snow persistence, while the grouping is an artifact of SWE amount. The group with lower daily mean DEAE values (WY2007, WY2008, WY2012, and WY2015) all have below-average SWE. Low SWE leads to fewer days of snow cover and that period of snow cover duration can be shortened further by the presence of dust in any concentration. Below-average peak SWE years with high dust concentrations (e.g., WY2012) will have the shortest snow cover duration and thus the shortest cumulative period of irradiance. However, during that short period the high dust concentration generates greater DEAE, leading to the negative correlation with cumulative irradiance. The second group of points indicates similar behavior for average or above-average amounts of SWE. Longer snow cover duration is possible with lower dust concentrations, which results in larger cumulative irradiance values yet lower daily mean DEAE.

There is also a negative linear correlation between cumulative springtime precipitation and daily mean visible DEAE (Figure 10D). Spring precipitation falling as snow temporarily increases snow surface albedo, leading to low daily mean visible

DEAE over the ablation season (Figure 9; Figure 13). However, cumulative irradiance and dust concentration can modify that correlation. Years with low spring precipitation such as WY2012 and WY2018 had fewer temporary increases in snow surface albedo, yet both years also had low daily mean visible DEAE due to below-average incoming solar radiation (Figure 10). Additionally, WY2018 had lower dust concentration than WY2012 which likely resulted in lower DEAE despite receiving slightly more incoming solar radiation. Irradiance can also modify DEAE for years with high spring precipitation. WY2011 received the highest amount of spring precipitation, yet also had the highest cumulative irradiance driving increased daily mean DEAE.

### *2.5.3. Modeling of Snow Cover*

Values of  $\Delta$ SAG necessarily rely on the accurate representation of snowpack evolution by the energy balance model SNOBAL. Snowpack was simulated from approximate date of peak SWE through to the end of the ablation season, and not for the entire WY, to minimize divergence of modeled and observed snowpack. The energy balance simulation of accumulation is complex and would be subject to greater uncertainty due to rapidly-changing or inconsistent early-season snow state variables (e.g., snow depth). All SNOBAL simulations began at approximately peak SWE to use snow state variables from an established snowpack with enough bulk SWE to more successfully model energy and mass transfers. There are two consistent approximations made across all SNOBAL runs which may have influenced  $\Delta$ SAG results.

First, an upper limit on net solar radiation of  $800 \text{ W m}^{-2}$  is hardcoded into the model (Marks and Dozier, 1992) and could be affecting melt rate. This limit does not

accurately represent the radiation-dominated continental climate of the San Juan Mountains, which experience relatively high irradiances compared to other climates such as the cloudy Pacific Northwest (Painter et al., 2012). Every year of “dusty” model runs had days with maximum springtime net solar inputs greater than  $800 \text{ W m}^{-2}$ . However, the springtime daily mean net solar input for every “dusty” model run was less than  $500 \text{ W m}^{-2}$  so the effect on melt rates is likely limited (see Appendix B for individual WY net solar input summary).

Second, the SWE of spring snowfall seems to be consistently under-estimated resulting in either divergence between modeled and observed SWE (e.g., WY2011) or greater inaccuracy in modeled SAG (e.g., WY2019) (Figure 11). The model runs were initiated with state variables from a snow plot several meters away from the tower that supplied subsequent forcing variables, thus some divergence in SWE may be due to spatial variability of snow depth (Fassnacht et al., 2009). However, the prevalence of the under-estimation indicates a systemic error in precipitation inputs. In SNOBAL, precipitation has been partitioned to “rain” or “snow” based on dewpoint temperature and the snow percentages are based on monitoring in the Sierra Nevada (CA) (Susong et al., 1999; Marks et al., 1992). The dewpoint temperature is calculated from daily maximum and minimum temperatures and may not capture the dewpoint temperature at the specific time of a precipitation event, as the model has an hourly timestep. Based only on air temperature, there is variability in the temperature threshold between snow and rain for different climate zones (Fassnacht and Soulis, 2002; Rajagopal and Harpold, 2016); also, snow can fall at warmer air temperatures in the continental climate

of Colorado than in more humid or maritime environments (Fassnacht et al., 2013; Jennings et al., 2018).

Additionally, the fresh snow densities of the partitioning table are based on SNOTEL sites in the Wasatch Range (UT) (Susong et al., 1999). These densities may not be fully representative of the higher elevation, semi-arid climate of the San Juan Mountains (CO). In Colorado climate, fresh snow can have lighter density compared to wetter environments (Judson and Doesken, 2000; Meinhardt and Fassnacht, 2020).

The limit on net solar radiation and the underestimation of precipitation inputs may cancel out each other in their combined effects on  $\Delta$ SAG. The upper threshold on net solar radiation restricts the energy available to the modeled snowpack, slowing melt rates and lengthening snow persistence. However, the under-estimation of precipitation inputs results in lower bulk SWE which would have shorter snow cover duration regardless of dust presence.

#### *2.5.4. Potential Drivers of Snow Cover Duration*

We compared four independent variables to  $\Delta$ SAG in a series of simple logarithmic or linear regressions. These comparisons had varying degrees of significance ( $p$ -values in Table 5) reflected in our summary of correlations in Section 2.4.4. One-variable comparisons cannot represent complex natural systems, so these results should be understood as preliminary (for a glimpse of the multiple regression analysis we are currently exploring, see Appendix C). The exclusion of deviant years in these simple regressions could have been prone to “over-fitting” or arbitrary exclusion of data points to increase correlation coefficients. To avoid this, we attempted to exclude the minimum number of deviant years. There was also some consistency in the group of

deviant years excluded; when comparing  $\Delta$ SAG to dust characteristics WY2012 and WY2013 were identified as displaying atypical “dust response” and when comparing  $\Delta$ SAG to climate characteristics WY2009, WY2015, and WY2017 were identified as displaying atypical irradiance or precipitation behavior. We understood the patterns in Figure 12 to be a guide of correlation but not necessarily of causation.

Dust concentration and  $\Delta$ SAG have a logarithmic correlation which implies that increases in dust concentration lead to increased difference in snow cover duration for “dusty” compared to “clean” snowpack scenarios (Figure 12A). This relation can be modified by the magnitude of the seasonal snowpack. Below-average SWE implies shorter snow persistence regardless of dust, which results in lower  $\Delta$ SAG (Skiles et al., 2012) as seen in WY2012 and WY2013. Peak SWE for WY2012 (561mm) and WY2013 (566mm) are both below-average compared to the period of record (an average peak SWE of 719mm from WY2007 to 2019). High dust concentrations can be correlated to large changes in snow cover duration when the SWE amount is considered.

The number of dust events has a strong linear correlation to increased  $\Delta$ SAG (Figure 12B). Simplistically, more dust deposition events can correspond to heavier dust loading and contribute to increased difference in snow cover duration. However, WY2012, WY2013, and WY2018 all had below-average SWE driving shorter snow persistence despite above-average numbers of dust events. Additionally, the high number of dust events for WY2012 and WY2018 does not correspond to heavy dust loading as both years had end-of-year dust concentration below  $2\text{mg g}^{-1}$ . The number of dust events is only one component of dust loading and correlation with  $\Delta$ SAG should consider dust concentration and amount of SWE.

Generally, increases in cumulative springtime irradiance and precipitation are correlated to slight increases in  $\Delta$ SAG (Figure 12C, 12D). The correlation of springtime irradiance and  $\Delta$ SAG seems to be primarily driven by amount of SWE, with above-average peak SWE years receiving more cumulative irradiance and below-average peak SWE years receiving less due to length of snow cover duration. Similarly, the correlation of increased springtime precipitation and increased  $\Delta$ SAG can be attributed to spring snow events temporarily increasing snow surface albedo and adjusting snow persistence by adding to bulk SWE. However, dust concentration can influence the relation of irradiance and precipitation to  $\Delta$ SAG as illustrated by WY2009, WY2015, and WY2017. WY2009 is a high-dust year with a cloudy spring compared to other high-dust years (e.g., WY2010) yet experiences the largest  $\Delta$ SAG possibly due to a combination of above-average peak SWE leading into a spring with little new snow accumulation (Figure 13). WY2015 and WY2017 are low-dust years which received enough late-season precipitation to lengthen snow cover duration and inflate cumulative irradiance values (e.g., Figure 9). This corroborates the finding of Painter et al. (2007) that greater SWE accumulation allows a longer period of dust influence, leading to greater divergence in snow cover duration.

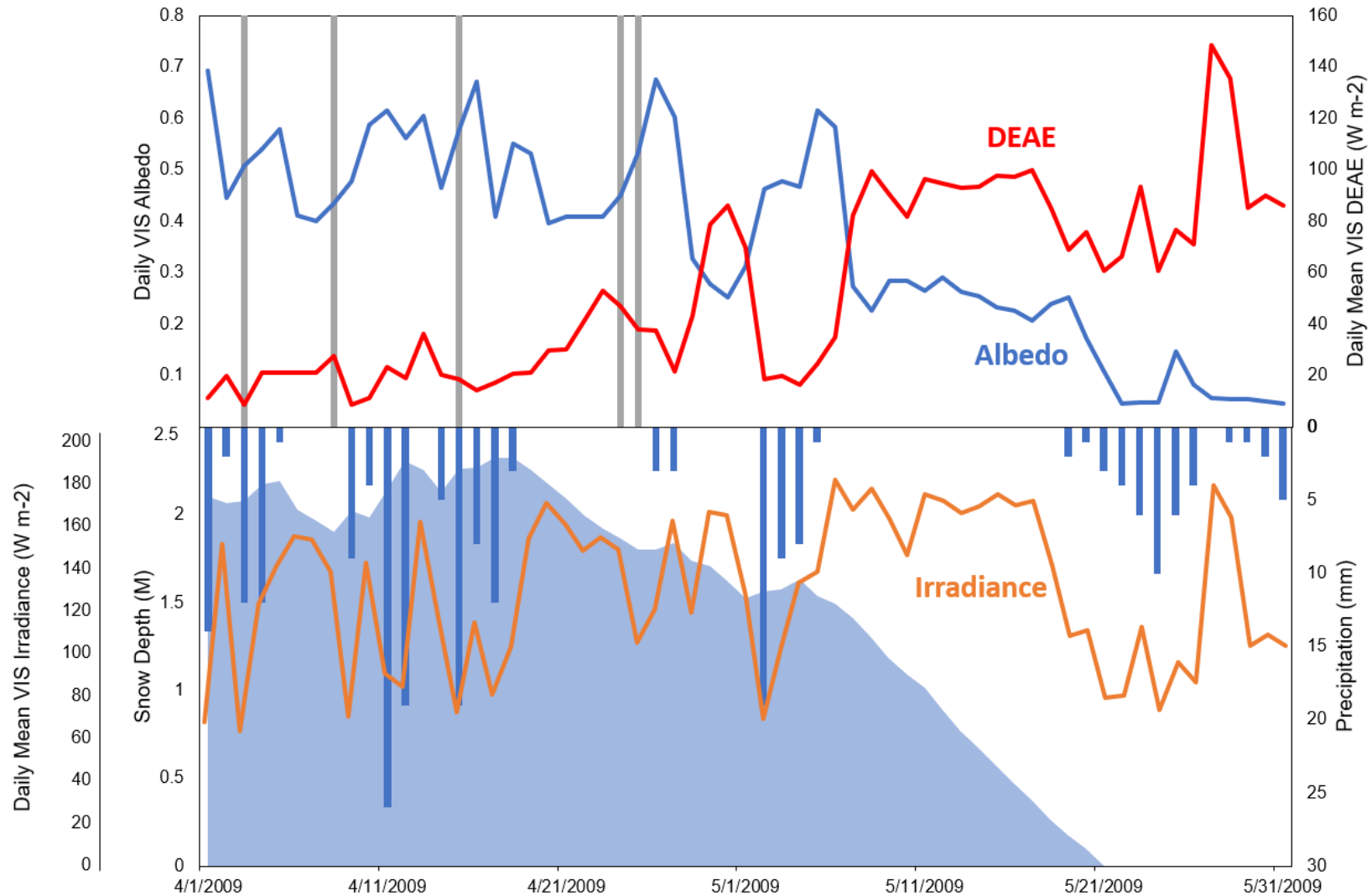


**Figure 13.** Snow surface albedo and daily mean visible DEAE (above) compared to snow depth, precipitation inputs, and visible irradiance (below) for April and May of WY2009. Vertical grey bars represent dust events. WY2009 was a high-dust year ( $4.7\text{mg g}^{-1}$  end-of-year dust concentration) with the largest  $\Delta\text{SAG}$  (31 days).

## 2.6. Conclusion

We found the daily mean visible DEAE to be primarily driven by end-of-year dust concentration with modifications from snow amount, springtime solar irradiance conditions and precipitation timing. The amount of dust-enhanced absorbed visible energy ranged from a daily mean of 31 to 51  $W m^{-2}$ . Calculated hourly visible DEAE was as high as 480  $W m^{-2}$ . Interannual variations in daily mean DEAE are primarily driven by variations in end-of-year dust concentrations.

Snow cover duration decreased under dusty conditions for all years modeled, with the range of melt acceleration from 11 to 31 days. Earlier melt was not directly driven by daily mean visible DEAE. The bulk amount of SWE influences snow cover duration, regardless of dust, and timing of springtime irradiance and precipitation can also influence snow cover melt rate. Our results emphasize that bulk seasonal averages of SWE, dust concentration, irradiance, and precipitation do not fully capture the sub-daily shifts in snow-dust-climate system dynamics leading to earlier snowmelt. Incorporation of individual dust layer burial depth, dispersal distance of dust layers throughout the snowpack, and the relative timing of irradiance and precipitation inputs would potentially improve simulations of snowmelt. Future development of operational streamflow forecasting for the UCRB will benefit from continued monitoring and quantification of those sub-seasonal effects.

### CHAPTER 3. IMPLICATIONS AND FUTURE WORK

Projected warming in the southwestern USA will increase potential drought, disturbance, and desertification (Munson et al., 2011) which can lead to increased dust loading of southwestern Colorado snowpack. Snow deposition timing and amount are also projected to become increasingly variable in the region (Barnett et al., 2006; Fyfe et al., 2017). We found that deposited dust layers can increase the mean visible energy absorbed by the snowpack up to an additional  $51 \text{ W m}^{-2}$  per day during ablation season in the UCRB. This accelerated melt from 11 to 31 days when only considering energy in the visible spectrum; previous studies have found melt advanced up to 51 days when also considering NIR/SWIR effects (Skiles et al., 2012).

Further investigation of the impact of dust on snowpack energy balance is needed since the connection between dust loading and melt acceleration is not direct. Skiles and Painter (2017) found a log-linear relation between dust concentrations and visible snow surface albedo, implying that even small increases in dust amount can lead to large decreases of albedo. Through this effect on snow surface albedo, dust in snow has been shown to increase the solar radiation absorbed by snowpack (Wiscombe and Warren, 1980; Painter et al., 2007; Skiles et al., 2012). This dust-enhanced radiative forcing has potentially shortened snow cover in southwestern Colorado by up to 51 days (Skiles et al., 2012) accelerating timing of snowmelt runoff in the region (Painter et al., 2010; Deems et al., 2013).

Timing and magnitude of snow deposition are projected to become increasingly variable in the Mountain West (Barnett et al., 2006; Fyfe et al., 2017). Additionally, drought conditions in the Colorado Plateau are expected to worsen with climate

warming, leading to increased desertification and aeolian dust transport (Nauman et al., 2018; Williams et al., 2020) and potentially increasing dust loading of snowpack in southwestern Colorado. The effect of dust on melt rates has already been shown to introduce bias in operational runoff predictions for the UCRB (Bryant et al., 2013; Painter et al., 2018). Accounting for the dust-enhanced radiative effect on the snowpack energy balance will somewhat reduce the uncertainty of runoff predictions (Follum et al., 2019).

Continued investigation of interannual and sub-seasonal patterns of dust loading is necessary to better inform operational snowmelt projections in the UCRB. Our results indicate that dust concentration magnitude is not directly responsible for accelerated melt rates and that sub-seasonal combinations of SWE magnitude, irradiance, and precipitation all influence snow cover duration. Daily analysis of dust, snow, and climate dynamics by Skiles and Painter (2017) over a high-dust and low-SWE ablation season (WY2013) showed that even small dust concentrations can decrease albedo and snow depth declined 50% faster than years of similar depth and lower dust. Understanding the relation of snowpack development and dust concentration may require measurements at a finer temporal resolution than bulk seasonal averages. There is also the need by water managers to expand beyond point-based studies and ascertain melt acceleration changes across larger basins. Bryant et al. (2013) proposed the adoption of the MODIS Dust Radiative Forcing in Snow product (MODDRFS) as a qualitative approximation of dust-enhanced absorbed energy that could be used to manually adjust melt factors in temperature-index models. However, MODDRFS determines the instantaneous radiative forcing by dust caused only by surface darkening and does not

capture the effects of accelerated snow grain growth. Future calibration of remote-sensing products and forecasting of melt acceleration will depend on direct monitoring of snowpack energy balance at multiple locations.

This research characterized historical point-based bulk snow and dust dynamics. Next steps would be to understand individual dust layer dynamics in relation to sub-seasonal snow and climate variables, to incorporate weather forecasts into snowpack energy balance modeling, and develop a real-time dust-enhanced energy absorption forecast product for operational end-users.

## REFERENCES

- Anderson, E. A. (1976), A point energy and mass balance model of a snow cover, *NOAA Tech. Rep. NWS, 19*, Natl. Oceanic and Atmos. Admin., Silver Spring, Md.
- Anghileri, D., N. Voisin, A. Castelletti, F. Pinaosi, B. Nijssen, and D. P. Lettenmaier (2016), Value of long-term streamflow forecasts to reservoir operations for water supply in snow-dominated river catchments, *Water Resour. Res.*, *52*, 4209-4225, doi: 10.1002/2015WR017864
- Bales, R. C., N. P. Molotch, T. H. Painter, M. D. Dettinger, R. Rice, and J. Dozier (2006), Mountain hydrology of the western United States, *Water Resour. Res.*, *42*, W08432, doi:10.1029/2005WR004387
- Barnhart, T. B., N. P. Molotch, B. Livneh, A. P. Harpold, J. F. Knowles, and D. Schneider (2016), Snowmelt rate dictates streamflow, *Geophys. Res. Lett.*, *43*, 8006-8016, doi:10.1002/2016GL069690
- Burnash, R. J., R. L. Ferral, and R. A. McGuire (1973), *A generalized streamflow simulation system conceptual modeling for digital computers*, U.S. Dept. of Commerce NWS and State of Calif. Dept. of Water Res.
- Clow, D. W. (2010), Changes in the timing of snowmelt and streamflow in Colorado: a response to recent warming, *J. Clim.*, *23*(9), 2293–2306, doi:10.1175/2009JCLI2951.1
- Deems, J. S., T. H. Painter, J. J. Barsugli, J. Belnap, and B. Udall (2013), Combined impacts of current and future dust deposition and regional warming on Colorado River Basin snow dynamics and hydrology, *Hydrol. Earth Syst. Sci.*, *17*, 4401-4413
- Dozier, J., R. O. Green, A. W. Nolin, T. H. Painter (2007), Interpretation of snow properties from imaging spectrometry, *Rem. Sens. Environ.*, *113*, doi:10.1016/j.rse.2007.07.029
- Fassnacht, S.R. and E. D. Soulis (2002), Implications during transitional periods of improvements to the snow processes in the land surface scheme-hydrological model WATCLASS, *Atmos-Ocean*, *40* (4), 389-403, doi:10.3137/ao.400402
- Fassnacht, S. R. (2004), Estimating Alter-shielded gauge snowfall undercatch, snowpack sublimation, and blowing snow transport at six sites in the coterminous USA, *Hydrol. Proc.*, *18* (18), 3481-3492. doi:10.1002/hyp.5806
- Fassnacht, S. R., M. W. Williams, and M. V. Carrao (2009), Changes in the surface roughness of snow from millimetre to metre scales, *Eco. Complex.*, *6*, 221-229, doi:10.1016/j.ecocom.2009.05.003
- Fassnacht, S.R., Venable, N. B. H., Khishigbayar, J., and M. L. Cherry (2013), The probability of precipitation as snow derived from daily air temperature for high elevation areas of Colorado, United States, *Int. Assoc. Hydrolog. Sci.*, *360*, 65-70
- Flanner, M. G. and C. S. Zender (2006), Linking snowpack microphysics and albedo evolution, *J. Geophys. Res.*, *111*, D12208, doi:10.1029/2005JD006834

- Flanner, M. G., C. S. Zender, P. G. Hess, N. M. Mahowald, T. H. Painter, V. Ramanathan, and P. J. Rasch (2009), Springtime warming and reduced snow cover from carbonaceous particles, *Atmos. Chem. Phys.*, *9*, 2481-2497
- Flanner, M. G., X. Liu, C. Zhou, J. E. Penner, and C. Jiao (2012), Enhanced solar energy absorption by internally-mixed black carbon in snow grains, *Atmos. Chem. Phys.*, *12*, 4699-4721, doi:10.5194/acp-12-4699-2012
- Follum, M. L., J. D. Niemann, and S. R. Fassnacht (2019), A comparison of snowmelt-derived streamflow from temperature-index and modified-temperature-index snow models, *Hydro. Proc.*, 1-16, doi: 10.1002/hyp.13545
- Franz, K. J., T. S. Hogue, S. Sorooshian (2008), Operational snow modeling: addressing the challenges of an energy balance model for National Weather Service forecasts, *J. of Hydrol.*, *360*, 48-66
- Gaupp, F., J. Hall, and S. Dadson (2015), The role of storage capacity in coping with intra- and inter-annual water variability in large river basins, *Environ. Res. Lett.*, *10*, 125001, doi: 10.1088/1748-9326/10/12/125001
- Harpold, A. A. and P. D. Brooks (2018), Humidity determines snowpack ablation under a warming climate, *Proc. Natl. Acad. Sci.*, *115* (6), 1215-1220, doi:10.1073/pnas.1716789115
- Hock, R. (2003), Temperature index melt modelling in mountain areas, *J. of Hydrol.*, *282*, 104-115
- Jennings, K.S., T. S. Winchell, B. Livneh, and N. Molotch (2018), Spatial variation of the rain-snow temperature threshold across the Northern Hemisphere, *Nature Comm.*, *9*, doi:10.1038/s41467-018-03629-7
- Judson, A. and N. Doesken (2000), Density of freshly fallen snow in the Central Rocky Mountains, *Amer. Meteorol. Soc.*, *81* (7), 1577-1587
- Landry, C. C., K. A. Buck, M. S. Raleigh, and M. P. Clark (2014), Mountain system monitoring at Senator Beck Basin, San Juan Mountains, Colorado: A new integrative data source to develop and evaluate models of snow and hydrologic processes, *Water Resour. Res.*, *50*, 1773-1788, doi:10.1002/2013WR013711
- Lawrence, C. R., T. H. Painter, C. C. Landry, and J. C. Neff (2010), Contemporary geochemical composition and flux of aeolian dust to the San Juan Mountains, Colorado, United States, *J. Geophys. Res.*, *115*, G03007, doi: 10.1029/2009JG001077
- López-Moreno, J. I., S. R. Fassnacht, J. T. Heath, K. N. Musselman, J. Revuelto, J. Latron, E. Morán-Tejeda, T. Jonas (2013), Small scale spatial variability of snow density and depth over complex alpine terrain: Implications for estimating snow water equivalent, *Adv. In Water Res.*, *55*, 40-52
- Marks, D. and J. Dozier (1992), Climate and energy exchange at the snow surface in the alpine region of the Sierra Nevada 2. Snow Cover Energy Balance, *Water Resour. Res.*, *28* (11), 3043-3054

- Marks, D., J. Domingo, D. Susong, T. Link, and D. Green (1999), A spatially distributed energy balance snowmelt model for application in mountain basins, *Hydrol. Proc.*, *13*, 1935-1959
- Marshall, A. M., J. T. Abatzoglou, T. E. Link, and C. J. Tennant (2019), Projected changes in interannual variability of peak snowpack amount and timing in the Western United States, *Geophys. Res. Lett.*, *46* (15), 8882– 8892, doi:10.1029/2019GL083770
- Martinec, J., A. Rango, and R. Roberts (2008), Snowmelt Runoff Model User's Manual, Updated Edition 2008, WinSRM Version 1.11. New Mexico State University Agricultural Experiment Station, Special Report 100
- Meinhardt, M. and S. R. Fassnacht (2020), Fresh Snow Density from the Fort Collins Colorado Meteorological Station and New Measurements, *Colorado Water*
- Melloh, R. A., J. P. Hardy, R. E. Davis, and P. B. Robinson (2001), Spectral albedo/reflectance of littered forest snow during the melt season, *Hydrol. Proc.*, *15*, 3409-3422
- Moriassi, D. N., J. G. Arnold, M. W. Van Liew, R. L. Bingner, R. D. Harmel, T. L. Veith (2007), Model evaluation guidelines for systematic quantification of accuracy in watershed simulations, *Trans. of the Amer. Soc. of Ag. and Biog. Engin.*, *50*(3), 885-900
- Munson, S. M., J. Belnap, and G. S. Okin (2011), Responses of wind erosion to climate-induced vegetation changes on the Colorado Plateau, *Proc. Natl. Acad. Sci. U. S. A.*, *108*, 3854-3859
- Musselman, K. N., M. P. Clark, C. Liu, K. Ikeda, and R. Rasmussen (2017), Slower snowmelt in a warmer world, *Nat. Clim. Change*, *7*, 214-220, doi: 10.1038/NCLIMATE3225
- Naumann, T. W., M. C. Duniway, N. P. Webb, and J. Belnap (2018), Elevated aeolian sediment transport on the Colorado Plateau, USA: The role of grazing, vehicle disturbance, and increasing aridity, *Earth Surf. Process. Landforms*, *43*, 2897-2914, doi: 10.1002/esp.4457
- Neff, J. C., A. P. Ballantyne, G. L. Farmer, N. M. Mahowald, J. L. Conroy, C. C. Landry, J. T. Overpeck, T. H. Painter, C. R. Lawrence, and R. L. Reynolds (2008) Increasing eolian dust deposition in the western United States linked to human activity , *Nature*, *1*, 189-195, doi: 10.1038/ngeo133
- Oerlemans, J. (2000), Analysis of a 3 year meteorological record from the ablation zone of Morteratschgletscher, Switzerland: Energy and mass balance, *J. Glaciol.*, *46*, 571-579
- Painter, T. H., A. P. Barrett, C. C. Landry, J. C. Neff, M. P. Cassidy, C. R. Lawrence, K. E. McBride, and G. L. Farmer (2007), Impact of disturbed desert soils on duration of mountain snow cover, *Geophys. Res. Lett.*, *34*, L12502, doi:10.1029/2007GL030284
- Painter, T. H., J. S. Deems, J. Belnap, A. F. Hamlet, C. C. Landry, and B. Udall (2010), Response of Colorado River runoff to dust radiative forcing in snow, *Proc. Natl. Acad. Sci.*, *107*, 17125-17130, doi:10.1073/pnas.0913139107
- Painter, T. H., A. C. Bryant, and S. M. Skiles (2012), Radiative forcing by light absorbing impurities in snow from MODIS surface reflectance data, *Geophys. Res. Lett.*, *39*, L17502, doi:10.1029/2012GL052457
- Painter, T. H., S. M. Skiles, J. S. Deems, A. C. Bryant, and C. C. Landry (2012), Dust radiative forcing in snow of the Upper Colorado River Basin: 1. A 6 year record of energy balance,

radiation, and dust concentrations, *Water Resour. Res.*, *48*, W07521, doi: 10.1029/2012WR011985

Painter, T. H., D. F. Berisford, J. W. Boardman, K. J. Bormann, J. S. Deems, F. Gehrke, A. Hedrick, M. Joyce, R. Laidlaw, D. Marks, C. Mattmann, B. McGurk, P. Ramirez, M. Richardson, S. M. Skiles, F. C. Seidel, and A. Winstral (2016), The Airborne Snow Observatory: Fusion of scanning lidar, imaging spectrometer, and physically-based modeling for mapping snow water equivalent and snow albedo, *Rem. Sens. Environ.*, *184*, 139-152, doi: 10.1016/j.rse.2016.06.018

Painter, T. H., S. M. Skiles, J. S. Deems, W. T Brandt, and J. Dozier (2017), Variation in rising limb of Colorado River snowmelt runoff hydrograph controlled by dust radiative forcing in snow, *Geophys. Res. Lett.*, *45*, 797-808, doi: 10.1002/2017GL075826

Rajagopal, S. and A. A. Harpold (2016), Testing and improving temperature thresholds for snow and rain prediction in the Western United States, *J. Amer. Water Res. Assoc.*, *52*(5), 1142-1154, doi:10.1111/1752-1688.12443

Reynolds, R. L., H. L. Goldstein, B. M. Moskowitz, A. C. Bryant, S. M. Skiles, R. F. Kolay, C. B. Flagg, K. Yauk, T. Berquó, G. Breit, M. Ketterer, D. Fernandez, M. E. Miller, and T. H. Painter (2014), Composition of dust deposited to snow cover in the Wasatch Range (Utah, USA): Controls on radiative properties of snow cover and comparison to some dust-source sediments, *Aeol. Res.*, *15*, 73-90, doi: 10.1016/j.aeolia.2013.08.001

Reynolds, R. L., H. L. Goldstein, B. M. Moskowitz, R. F. Kokaly, S. M. Munson, P. Solheid, G. N. Breit, C. R. Lawrence, and J. Derry (2020), Dust deposited on snow cover in the San Juan Mountains, Colorado, 2011-2016: Compositional variability bearing on snow-melt effects, *J. of Geophys. Res.: Atmos.*, *125*, 1-24, doi:10.1029/2019JD032210

Seidel, F. C., K. Rittger, S. M. Skiles, N. Molotch, and T. H. Painter (2016), Case study of spatial and temporal variability of snow cover, grain size, albedo and radiative forcing in the Sierra Nevada and Rocky Mountain snowpack derived from imaging spectroscopy, *The Cryosph.*, *10*, 1299-1244

Skiles, S. M., T. H. Painter, J. S. Deems, A. C. Bryant, and C. C. Landry (2012), Dust radiative forcing in snow of the Upper Colorado River Basin: 2. Interannual variability in radiative forcing and snowmelt rates, *Water Resour. Res.*, *48*, W07522, doi: 10.1029/2012WR011986

Skiles, S. M. (2014), Dust and black carbon radiative forcing controls on snowmelt in the Colorado River basin (doctoral dissertation) in: Geography, Univ. of Calif.-Los Angeles

Skiles, S. M., T. H. Painter, J. Belnap, L. Holland, R. L. Reynolds, H. L. Goldstein, and J. Lin (2015), Regional variability in dust-on-snow processes and impacts in the Upper Colorado River Basin, *Hydro. Proc.*, *29*, 5397-5413, doi: 10.1002/hyp.10569

Skiles, S. M and T. Painter (2017), Daily evolution in dust and black carbon content, snow grain size, and snow albedo during snowmelt, Rocky Mountains, Colorado, *J. Glaciol.*, *63* (237), 118-132

Skiles, S. M., M. Flanner, J. M. Cook, M. Dumott, and T. Painter (2018), Radiative forcing by light-absorbing particles in snow, *Nat. Clim. Change*, *8*, 964-971, doi: 10.1038/s41558-018-0296-5

- Stewart, I. T., D. R. Cayan, and M. D. Dettinger (2004), Changes toward earlier streamflow timing across Western North America, *J. Clim.*, 18, 1136-1155, doi:10.1175/JCLI3321.1
- Susong, D., D. Marks, and D. Garen (1999), Methods for developing time-series climate surfaces to drive topographically distributed energy- and water-balance models, *Hydrol. Proc.*, 13, 2003-2021
- Thomas, C. W. (1963), On the transfer of visible radiation through sea ice and snow, *J. of Glaciol.*, 4 (34), 481-484
- Trujillo, E. and N. Molotch (2014), Snowpack regimes of the Western United States, *Water Resour. Res.*, 50, 5611-5623
- Warren, S. G. and W. J. Wiscombe (1980), A model for the spectral albedo of snow, II: Snow containing atmospheric aerosols, *J. Atmos. Sci.*, 37, 2734-2745, doi:10.1175/1520-0469(1980)037<2734:AMFTSA>2.0CO;2
- Williams, A. P., E. R. Cook, J. E. Smerdon, B. I. Cook, J. T. Abatzoglou, K. Bolles, S. H. Baek, A. M. Badger, and B. Livneh (2020), Large contribution from anthropogenic warming to an emerging North American megadrought, *Sci.*, 368 (6488), 314-318, doi:10.1126/science.aaz9600
- Wilson, L. L., L. Tsang, J. Hwang, and C. Chien (1999), Mapping snow water equivalent by combining a spatially distributed snow hydrology model with passive microwave remote-sensing data, *IEEE Trans. Geosci. Rem. Sens.*, 37, 690-704, doi:10.1109/36.752186
- Wiscombe, W. J. and S. G. Warren (1980), A model for the spectral albedo of snow, I: Pure snow, *J. Atmos. Sci.*, 37, 2712-2732, doi: 10.1175/1520-0469(1980)037<2712:AMFTSA>2.0CO;2

## APPENDIX A. DATASETS

**Table A-1.** Instrumentation at CSAS meteorological towers (from Landry et al., 2014)

<b>Variable</b>	<b>Sensor</b>	<b>Units</b>
Precipitation <sup>a</sup>	ETI Noah II	mm
Wind speed and direction	RM Young Wind Monitor 05103-5	meters per second
Air temperature	Vaisala HMP50YA (SB, SA), Vaisala CS500 (SA)	Celsius
Humidity	Vaisala HMP50YA (SB, SA), Vaisala CS500 (SA)	percentage
Incoming solar radiation (broadband)	Kipp & Zonen CM21 Pyranometer	Watts per m <sup>2</sup>
Incoming solar radiation (NIR/SWIR)	Kipp & Zonen CM21 RG695 NIR/SWIR Pyranometer	Watts per m <sup>2</sup>
Diffuse incoming solar radiation	Kipp & Zonen CM21 RG695 NIR/SWIR Pyranometer (SB), Swiss ASRB Shadow Arm (SA)	Watts per m <sup>2</sup>
Incoming thermal radiation	Kipp & Zonen CG-4 Pyrgeometer	Watts per m <sup>2</sup>
Barometric pressure	Vaisala PTB101B (SA)	millibars
Snow depth	CSI SR50 ultrasonic distance ranger	meters
Reflected solar radiation (broadband)	Kipp & Zonen CM21 Pyranometer	Watts per m <sup>2</sup>
Reflected solar radiation (NIR/SWIR)	Kipp & Zonen CM21 RG695 NIR/SWIR Pyranometer	Watts per m <sup>2</sup>
Infrared snow surface temperature	AlpuG SnowSurf	Celsius

<sup>a</sup> only collected at SA site

**Sub-alpine plot 1-, 3-, and 24-hour datasets:**

< <https://snowstudies.org/archived-data/> >

**Alpine plot 1-, 3-, and 24-hour datasets:**

< <https://snowstudies.org/archived-data/> >

**CSAS Sensor Status Workbooks (Snow Stake Array Depths dataset):**

< <https://snowstudies.org/archived-data/> >

**CSAS Snow Pit Profile archive for SBB:**

< <http://www.codos.org/sbb#snowprofiles-sbb> >

**Red Mountain Pass SNOTEL dataset:**

< <https://wcc.sc.egov.usda.gov/nwcc/site?sitenum=713> >

APPENDIX B. INDIVIDUAL MODEL RESULTS

**Table B-1.** SNOBAL model run results under “dusty” scenario (actual conditions)

WY	Start pit date	Days of snow modeled	Modeled SAG	Observed SAG
2007	4/18/2007	49	6/5/2007	6/5/2007
2008	4/14/2008	65	6/17/2008	6/16/2008
2009	4/15/2009	38	5/21/2009	5/21/2009
2010	4/12/2010	48	5/30/2010	5/29/2010
2011	4/11/2011	74	6/24/2011	6/23/2011
2012	4/16/2012	26	5/12/2012	5/11/2012
2013 <sup>a</sup>	4/16/2013	31	5/16/2013	5/18/2013
2014	4/16/2014	49	6/3/2014	6/6/2014
2015	4/14/2015	63	6/15/2015	6/15/2015
2016 <sup>a</sup>	4/13/2016	54	6/5/2016	6/9/2016
2017	4/6/2017	64	6/8/2017	6/10/2017
2018	4/8/2018	36	5/13/2018	5/16/2018
2019	3/26/2019	75	6/9/2019	7/10/2019

a = upper limit of Net Solar input parameter was set to 800 W m<sup>-2</sup>

**Table B-2.** SNOBAL model run results under “clean” conditions (where net solar input was decreased according to DEAE to simulate dust-free conditions)

WY	Start pit date	Days of snow modeled	Modeled SAG
2007	4/18/2007	68	6/25/2007
2008	4/14/2008	88	7/10/2008
2009	4/15/2009	69	6/22/2009
2010	4/12/2010	71	6/21/2010
2011 <sup>a</sup>	4/11/2011	101	7/21/2011
2012	4/16/2012	39	5/25/2012
2013	4/16/2013	49	6/3/2013
2014	4/16/2014	73	6/27/2014
2015	4/14/2015	74	6/26/2015
2016	4/13/2016	73	6/25/2016
2017	4/6/2017	78	6/23/2017
2018	4/8/2018	50	5/27/2018
2019	3/26/2019	98	7/2/2019

a = upper limit of Net Solar parameter was set to 800 Wm<sup>-2</sup>

**Table B-3.** RMSE and NSE results for modeled dusty SWE compared to observed

WY	Daily derived SWE curves		Irregular manual measured SWE	
	RMSE (mm)	NSE	RMSE (mm)	NSE
2007	64	0.89	59	0.91
2008	120	0.81	26	0.98
2009	57	0.95	35	0.94
2010	60	0.86	30	0.94
2011	91	0.90	80	0.79
2012	59	0.76	20	0.97
2013	37	0.97	156	-2.45
2014	58	0.89	119	0.64
2015	70	0.67	49	0.87
2016	70	0.93	119	-1.96
2017	52	0.92	108	0.46
2018	85	0.53	98	-4.80
2019	287	-0.19		
overall				

**Table B-4.** Maximum net solar springtime inputs (over 1 April to June 30) and springtime daily mean net solar input (taken from 0900 to 1700 hours)

WY	Dusty Scenario		Clean Scenario	
	Maximum Net Solar (W m-2)	Daily Mean Net Solar (W m-2)	Maximum Net Solar (W m-2)	Daily Mean Net Solar (W m-2)
2007	1006	349	535	221
2008	981	349	528	230
2009	1024	381	548	221
2010	1004	407	530	243
2011	942	311	513	213
2012	999	469	537	270
2013	1016	460	548	261
2014	1016	375	534	229
2015	1105	319	567	208
2016	979	347	516	216
2017	999	389	522	244
2018	996	457	537	263
2019	931	291	494	199

APPENDIX C. MULTIPLE REGRESSION ANALYSIS

**Table C-1.** Cross-correlation ( $R^2$ ) between the independent variables

	Number of dust events	Cumulative springtime irradiance	Cumulative springtime precipitation	1 April SWE	Percent of dust events post-peak SWE
End-of-year dust concentration	0.293	0.172	0.094	0.008	0.001
Number of dust events		0.187	0.042	0.008	0.108
Cumulative springtime irradiance			<b>0.618</b>	<b>0.511</b>	0.006
Cumulative springtime precipitation				0.157	0.069
1 April SWE					0.143

**Table C-2.** Multi-variate linear regression results

	<b>ΔSAG</b>		<b>Daily mean visible DEAE</b>	
Constant	-11.1	-12.5	14.8	19.9
End-of-year dust concentration	2.42	2.48	6.11	5.91
Number of dust events	15.6	17.2	10.8	5.15
Precipitation	7.06	3.73	-20.6	-8.53
1 April SWE	31.3	28.9	18.9	27.3
Percent of dust events post peak SWE	-4.95	-5.64	-3.05	-0.551
Irradiance	-6.26		22.7	
Adjusted $R^2$	0.884	0.895	0.688	0.654
NSE	0.942	0.939	0.844	0.798
Standard error	2.02	1.92	3.01	3.18